JGR Atmospheres

RESEARCH ARTICLE
10.1029/2018JD029614

Preferential Deposition of Snow and Dust Over Hills: Governing Processes and Relevant Scales

F. Comola[1], M. G. Giometto[2], S. T. Salesky[3], M. B. Parlange[4], and M. Lehning[1,5]

[1]School of Architecture, Civil and Environmental Engineering, École Polytechnique Fédérale de Lausanne, Lausanne, Switzerland, [2]Department of Civil Engineering and Engineering Mechanics, Columbia University, New York, NY, USA, [3]School of Meteorology, The University of Oklahoma, Norman, OK, USA, [4]Department of Civil Engineering, Monash University, Melbourne, Victoria, Australia, [5]WSL Institute for Snow and Avalanche Research SLF, Davos, Switzerland

Key Points:
- Snow and dust preferential deposition patterns depend on the length and velocity scales of interest
- Deposition maxima are located either on the windward or the leeward slope depending on the particle Froude and Stokes numbers
- The assumption of inertialess particles can only be justified for complex snowflake geometries

Correspondence to:
F. Comola,
francesco.comola@epfl.ch

Citation:
Comola, F., Giometto, M. G., Salesky, S. T., Parlange, M. B., & Lehning, M. (2019). Preferential deposition of snow and dust over hills: Governing processes and relevant scales. *Journal of Geophysical Research: Atmospheres*, *124*, 7951–7974. https://doi.org/10.1029/2018JD029614

Received 6 SEP 2018
Accepted 17 JUN 2019
Accepted article online 4 JUL 2019
Published online 24 JUL 2019

Abstract Preferential deposition of snow and dust over complex terrain is responsible for a wide range of environmental processes and accounts for a significant source of uncertainty in the surface mass balances of cold and arid regions. Despite the growing body of literature on the subject, previous studies reported contradictory results on the location and magnitude of deposition maxima and minima. This study aims at unraveling the governing processes of preferential deposition in a neutrally stable atmosphere and to reconcile seemingly inconsistent results of previous works. For this purpose, a comprehensive modeling approach is developed, based on large eddy simulations of the turbulent airflow, Lagrangian stochastic model of particle trajectories, and immersed boundary method to represent the underlying topography. The model is tested against wind tunnel measurements of dust deposition around isolated and sequential hills. A scale analysis is then performed to investigate the dependence of snowfall deposition on the particle Froude and Stokes numbers, which fully account for the governing processes of inertia, flow advection, and gravity. Model results suggest that different deposition patterns emerge from different combinations of dimensionless parameters, with deposition maxima located either on the windward or the leeward slope of the hill. Additional simulations are performed, to test whether the often used assumption of inertialess particles yields accurate deposition patterns. Results indicate that this assumption can be justified when snowflakes present dendritic shape but may generate unrealistic results for rounded particles. We finally show that our scale analysis provides qualitatively similar results for hills with different aspect ratios.

1. Introduction

The spatial variability of snowfall deposition over complex terrain is one of the larger unknowns in the surface mass balance of alpine and polar regions (Grünewald et al., 2010; Lenaerts et al., 2012) and is caused by physical processes acting at different spatial scales (Mott et al., 2014). At large scales, orographic precipitation is likely to be larger on the windward side of mountain ranges, where cloud formation is enhanced by updrafts of moist air (Houze, 2012). At intermediate scales, an increase of precipitation around the mountain top may occur due to the seeder-feeder mechanism, consisting of accretion of precipitation particles formed in an upper-level cloud that fall through a lower-level cloud capping the mountain top (Choularton & Perry, 1986). At smaller scales, a uniform precipitation above the surface may lead to a inhomogeneous deposition due to near-surface flow-particle interactions, the so-called preferential deposition (Orlandini & Lamberti, 2000; Zängl, 2008). The importance of this last process with respect to the larger-scale precipitation gradients was confirmed by Scipión et al. (2013) through radar measurements and more recently by Gerber et al. (2019) through numerical modeling.

The concept of preferential deposition was first introduced by Lehning et al. (2008) and has thus far been investigated in the context of snowfall deposition. However, the same physical process is relevant to deposition of other heavy particles. Wind-blown volcanic ashes and desert dust deposit on snow-covered mountain regions at global scale, causing a decrease in surface albedo and a faster snow melt (Di Mauro et al., 2018; Painter et al., 2010). Moreover, dust deposition on complex landforms provides a fundamental supply of nutrients to a variety of ecosystems, whose long-term productivity is limited by the availability of dustborne phosphorus (Kok et al., 2012; Okin et al., 2004).

Despite the recent advances in our understanding of preferential deposition, the effects of near-surface flow, particle properties, and topography have not been clearly identified. Because field measurements do not allow us to separate the effect of preferential deposition from those of precipitation gradients, wind-driven erosion and deposition, and microphysical processes (Gerber et al., 2017; Vionnet et al., 2017), research in the field relies to a great extent on mathematical modeling. However, results from previous numerical studies are not entirely consistent.

The first numerical models of preferential deposition adopted a simplified description of the transport process, based on a stationary form of the advection-diffusion equation that does not include the effect of particle inertia (Lehning et al., 2008; Mott & Lehning, 2010; Mott et al., 2010). These studies suggested that on the windward side of a mountain strong updrafts reduce the settling velocity of the particles, leading to a reduced deposition. This, in turn, generates an increase of particle concentration in the air that flows uphill toward the hilltop. Once on the leeward side, the reduced wake velocity and the large particle concentration induce a local increase of deposition.

More recent numerical studies that included the effect of particle inertia only partially supported these initial results. Salesky et al. (2019) showed that the effect of particle inertia leads to a larger snow deposition on the windward side, while Wang and Huang (2017) suggested that the deposition on the leeward side increases with increasing flow advection. The reason for such differences may be that particle dynamics depend on the interplay among flow advection, gravity, and particle inertia, which may vary with flow velocity and height of surface features.

Further elements of uncertainty include the small-scale interaction between turbulent flows and nonspherical particles (see, e.g., the review by Voth & Soldati, 2017). This problem is particularly relevant for snowflakes, which present a remarkable variety of size and shape depending on the atmospheric conditions upon formation (Nakaya, 1954). Parameterizations of the drag coefficient for dendritic crystals have been proposed in the literature (Loth, 2008) and adopted to investigate snow particle trajectories in turbulent flows (Huang et al., 2011). However, the influence of snow particle shape on preferential deposition has never been investigated before.

Here, we aim to provide a more comprehensive understanding of preferential deposition over hills and reconcile the seemingly inconsistent results of previous studies. Specifically, we perform a series of numerical experiments to test the sensitivity of the deposition pattern to the Froude and Stokes numbers, the two dimensionless parameters that characterize the dynamics of heavy particles in neutrally stable atmospheric flows. Furthermore, we provide insight into the sensitivity of the deposition process to the particle shape and inertia in boundary layer flow over an idealized Gaussian hill. A sensitivity analysis is also performed with respect to the aspect ratio of the Gaussian hill, that is, to the ratio between its height and standard deviation.

For this purpose, we develop a novel and comprehensive modeling framework based on large eddy simulations (LES) of the flow field and a Lagrangian stochastic model (LSM) of particle trajectories. We account for the form drag exerted by the surface topography on the surrounding flow through an immersed boundary method (IBM).

In section 2, we provide the details of the LES-LSM model developed for this study and introduce the dimensionless formulation of the particle transport equations. In section 3, we test the model results against wind tunnel measurements of dust deposition over Gaussian hills. In section 4, we describe the model setup and the simulations performed for the scale analysis. In section 5, we present the results of the scale analysis and the sensitivity analysis to particle shape, particle inertia, and hill aspect ratio. Discussion and concluding remarks will follow.

2. Methods

2.1. LES

The LES approach aims at resolving the energy-containing scales of the turbulent flow while providing an appropriate model for the effects of the small-scale motions (Pope, 2000). These small scales ideally belong to the inertial subrange, whose dynamics present well-known characteristics and thus allow us to

develop effective parameterizations. We adopt a LES model that solves the isothermal filtered Navier-Stokes equations (Orszag & Pao, 1975) for incompressible flows

$$\frac{\partial \tilde{u}_i}{\partial t} + \tilde{u}_j\left(\frac{\partial \tilde{u}_i}{\partial x_j} - \frac{\partial \tilde{u}_j}{\partial x_i}\right) = -\frac{\partial \tilde{\pi}}{\partial x_i} - \frac{\partial \tau_{ij}^{\mathrm{SGS}}}{\partial x_j} - \Pi_1 + \tilde{F}_i^{\Gamma_s} + \tilde{F}_i^{p} \qquad \text{in} \quad \Omega \times [0,T], \tag{1a}$$

$$\frac{\partial \tilde{u}_i}{\partial x_i} = 0 \quad \text{in} \quad \Omega \times [0,T], \tag{1b}$$

$$\frac{\partial \tilde{u}_1}{\partial x_3} = \frac{\partial \tilde{u}_2}{\partial x_3} = \tilde{u}_3 = 0 \quad \text{in} \quad \Gamma_t \times [0,T], \tag{1c}$$

$$(\tilde{\mathbf{u}} \cdot \tilde{\mathbf{n}})\tilde{\mathbf{n}} = \tilde{\mathbf{u}}_n = 0 \quad \text{in} \quad \Gamma_s \times [0,T], \tag{1d}$$

$$\tau_w = -\left[\frac{\kappa(||\tilde{\mathbf{u}} - \tilde{\mathbf{u}}_n||)}{\ln\left(1 + \frac{\Delta}{z_0}\right)}\right]^2 \quad \text{in} \quad \Gamma_s \times [0,T]. \tag{1e}$$

In equations (1), the tilde indicates spatially filtered quantities. $\tilde{u}_i$ are the velocity components in the three Cartesian directions ($i = 1, 2, 3$), $\tilde{\pi} = \tilde{p}/\rho_f + 1/3\,\tau_{ii}^{SGS} + 1/2\,\tilde{u}_i\tilde{u}_i$ is a modified filtered pressure field, and ρ_f is a reference density. The contribution $1/2\,\tilde{u}_i\tilde{u}_i$ in the modified pressure field derives from expressing the advection term in rotation form, which ensures conservation of kinetic energy in the discrete system (Moin & Kim, 1982). Π_1 is a fixed pressure gradient that we impose to drive the flow, and τ_{ij}^{SGS} is the subgrid scale stress tensor. Further, $\tilde{F}_i^{\Gamma_s}$ is a volumetric forcing term arising from the immersed boundary method; $\tilde{F}_i^{p}$ is a volumetric forcing term that includes the effect of inertial particles on the filtered flow; $\tilde{\mathbf{n}}$ is the surface normal vector; $\tilde{\mathbf{u}}_n$ is the normal-to-surface velocity vector, and τ_w the stress magnitude over fully rough surface.

Equation (1e) expresses the equilibrium logarithmic law of the wall, which is applied at the surface Γ_s to evaluate tangential-to-surface stresses in LES. $\kappa = 0.41$ is the von Kármán constant, $\Delta = \left(\Delta_x \times \Delta_y \times \Delta_z\right)^{1/3}$ is the width of the LES spatial filter, and z_0 is the aerodynamic roughness. The surface stress τ_w is calculated by applying the logarithmic law of the wall in the direction $\tilde{\mathbf{n}}$ normal to the surface, that is, based on the value of tangential velocity $\tilde{\mathbf{u}} - \tilde{\mathbf{u}}_n$ evaluated at distance Δ from the surface. Although the assumptions underlying the law of the wall do not hold in case of separated flow, previous studies (e.g., Kaimal & Finnigan, 1994) showed that equation (1e) is able to provide reliable simulations of turbulent flow over hills. The use of a simple algebraic wall model is in fact justified when considering that most of the surface drag is due to the resolved pressure field around the hill, and the tangential stresses (those we model via the wall law) are a minor contribution. A schematic representation of the system is shown in Figure 1.

This version of the LES and its wall model were tested and adopted to investigate the performance of a number of SGS models (Bou-Zeid et al., 2005; Meneveau et al., 1996; Porté-Agel et al., 2000), land-atmosphere interactions (Albertson & Parlange, 1999), wind-farm effects on the atmospheric boundary layer (Sharma et al., 2016), turbulent flows over realistic urban canopy layers (Giometto et al., 2017, 2016), and drifting snow sublimation (Sharma et al., 2018).

We solve the equations on a regular domain Ω using a pseudo spectral collocation approach (Orszag & Pao, 1975) in the horizontal directions and a staggered second-order accurate centered finite differences scheme in the vertical direction. We perform the time integration in the interval $[0, T]$ adopting a fully explicit second-order accurate Adams-Bashforth scheme and employ a fractional step method to compute the pressure field. We apply different conditions at the partitions of the computational boundary $\partial\Omega = \Gamma_s \cup \Gamma_t \cup \Gamma_l$, that is, a stress-free boundary conditions at the upper boundary Γ_t (equation (1c)), no-slip impermeable wall at the surface Γ_s (equation (1d)), and periodic conditions at the lateral boundaries Γ_l due to the Fourier expansions used in the pseudo spectral approach.

We rely on the static Smagorinsky closure model to evaluate τ_{ij}^{SGS}. This model evaluates the SGS terms as functions of the resolved-scale strain rate tensor

$$\tau_{ij}^{\mathrm{SGS}} = -2\nu_t\tilde{S}_{ij} = -2\left(c_s\Delta\right)^2|\tilde{S}|\tilde{S}_{ij}, \tag{2}$$

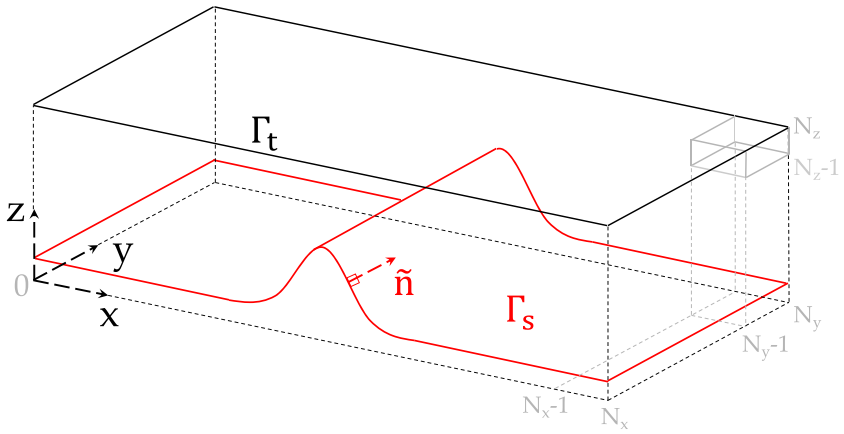

Figure 1. Schematic representation of the computational domain. Γ_t indicates the upper boundary and Γ_s the immersed boundary, here represented as a Gaussian ridge. The logarithmic law of the wall, equation (1e), is applied in the direction ñ normal to the surface. N_x, N_y, and N_z indicate the number of nodes of the Cartesian grid in the x, y, and z directions.

where ν_t is the eddy viscosity, $\tilde{S}_{ij}$ is the filtered strain rate tensor, and c_s is the Smagorinsky coefficient. Although a constant value $c_s = 0.16$ can be theoretically derived in case of homogeneous, isotropic turbulence with a sharp spectral cutoff filter (Lilly, 1967), this value is known to be overdissipative in LES of shear flows and models of boundary layer turbulence normally adopt $c_s = 0.1$. Because c_s should approach 0 in the near wall region, we adopt a wall damping function (Mason & Thomson, 1992) to avoid overdissipation of turbulence kinetic energy. The Smagorinsky coefficient has the following expression

$$c_s^2(x,y,z) = \left[c_0^{-n} + \frac{\Delta}{k\left(\tilde{\Psi}(x,y,z) + z_0\right)^n} \right]^{-\frac{2}{n}}, \tag{3}$$

where $c_0 = 0.1$, $n = 2$ is a calibration parameter suggested by Mason and Thomson (1992), and $\tilde{\Psi}(x,y,z)$ is the distance function from the surface (see section 2.2 for more details). According to equation (3), c_s approaches c_0 in the outer region, deviates significantly from c_0 at $\tilde{\Psi}(x,y,z) \approx \Delta^{1/n}$, and approaches 0 in the close vicinity of the surface.

2.2. Immersed Boundary Method

We represent the complex topography $\Gamma_s(x,y)$ by adopting a signed distance (or level set) function $\tilde{\Psi}(x,y,z)$, such that the computational domain is partitioned in two regions, that is, the below-surface region Ω_s where $\tilde{\Psi}(x,y,z) < 0$, and the above-surface region Ω_f where $\tilde{\Psi}(x,y,z) > 0$. The surface topography is then identified by the zero level set $\tilde{\Psi}(x,y,z) = 0$. Our implementation of the immersed boundary method is similar to the one proposed in Chester et al. (2007) and has been recently used to investigate the characteristics of urban canopy layers (Giometto et al., 2017, 2016).

We fix the velocity field to zero in the inside region Ω_s and enforce the law of the wall in all the grid nodes that fall in the region $-1.1\Delta < \tilde{\Psi}(x,y,z) < 1.1\Delta$. We do this by interpolating the tangential flow velocity $\tilde{\mathbf{u}} - \tilde{\mathbf{u}}_n$ at distance $\Delta + z_0$ from the grid node in the direction normal to the surface and calculating the tangential stress τ_w with equation (1e). Because the solution of equations (1a)–(1e) is of class C^0 in a given horizontal plane intersecting the surface, that is, with discontinuous first derivatives, the spectral representation of the flow field results in Gibbs phenomenon, which is characterized by oscillations with progressively increasing amplitude as the surface is approached. To mitigate this drawback, we perform a Laplacian smoothing of the velocity field in Ω_s before the spectral differentiation step, similar to that first proposed in Tseng et al. (2006). Therein, the smoothing algorithm was thoroughly tuned and tested in flow over a squared cylinder, where it proved to yield accurate results for this class of problems (see also Fang et al., 2011).

2.3. LSM

The LSM provides us with an evolution equation to model the SGS velocity of fluid parcels in turbulent flows. Used in combination with the LES technique, it allows us to account for the full turbulence spectrum and to thus perform accurate simulations of particle dispersion. We implement a modified version of

the LSM proposed by Thomson (1987). Therein, the author derived a stochastic evolution equation for the velocity fluctuations of a fluid parcel based on the local ensemble-mean velocity and velocity variances of the flow. Here, we replace the ensemble-mean velocity with the LES-resolved velocity and calculate the velocity variances based on the SGS closure model. A similar LSM approach was previously used to simulate the dispersion of passive tracers in a convective boundary layer (Weil et al., 2004) and the aeolian transport of snow particles (Zwaaftink et al., 2014).

If the SGS velocity component is isotropic, as commonly assumed in LES closure models, we can express the evolution of the SGS velocity along a fluid particle's trajectory $\mathbf{X}_f$ as

$$\mathrm{d}U_i^{\mathrm{SGS}} = -\frac{\alpha U_i^{\mathrm{SGS}}}{T_f}\mathrm{d}t + \frac{1}{2}\left(\frac{1}{\sigma^2}\frac{\mathrm{d}\sigma^2}{\mathrm{d}t}U_i^{\mathrm{SGS}} + \frac{\partial\sigma^2}{\partial x_i}\right)\mathrm{d}t + \left(\frac{\alpha 2\sigma^2}{T_f}\right)^{1/2}\mathrm{d}\xi_i, \tag{4}$$

where $\sigma^2 = 2e/3$ is the SGS velocity variance, which is directly proportional to the SGS turbulence kinetic energy (Pope, 2000)

$$e = \left(\frac{\epsilon\Delta}{c_\epsilon}\right)^{2/3}, \tag{5}$$

with ϵ is the energy dissipation rate, Δ is the width of the LES spatial filter, and $c_\epsilon = 0.93$ in neutral and unstable conditions. We compute the turbulence dissipation ϵ assuming that the mean energy production equals the mean energy dissipation (Kolmogorov, 1941). We thus perform a time average of the energy production term P over intervals of one eddy turnover time $T_e = L_z/u_\tau$, where L_z is the height of the computational domain and u_τ the average friction velocity. We then compute the energy dissipation in each grid node as

$$\epsilon \approx \langle P\rangle = \langle -\tau_{ij}\tilde{S}_{ij}\rangle. \tag{6}$$

In equation (4), $\alpha \in [0;1]$ is the SGS fraction of the total turbulence kinetic energy, that is, $\alpha = e/(e+k)$; e is given by equation (5) and k is the resolved turbulence kinetic energy

$$k = \frac{1}{2}\langle u_i' u_i'\rangle, \tag{7}$$

where angle brackets indicate time averaging and $u_i' = \tilde{u}_i - \langle\tilde{u}_i\rangle$ are the turbulent fluctuations. Further, $\mathrm{d}\xi_i \sim \mathcal{N}(0,\mathrm{d}t)$ is a random number sampled from a normal distribution of zero mean and variance $\mathrm{d}t$. $T_f = 2\sigma^2/C_0\epsilon$ is the Lagrangian velocity autocorrelation timescale, with $C_0 \approx 4$ (Weil et al., 2004).

Because the trajectory of a heavy particle does not generally coincide with a fluid parcel's trajectory, equation (4) should be modified to predict the turbulence fluctuations along the heavy particle's trajectory. For this purpose, Wilson (2000) suggested a reduction of the Lagrangian velocity autocorrelation timescale T_f. We therefore replace T_f with T_p (Wilson, 2000)

$$T_p = \frac{T_f}{\sqrt{1 + \frac{(\beta U_{p,3})^2}{\sigma^2}}}, \tag{8}$$

where $U_{p,3}$ is the vertical component of the Lagrangian particle velocity; $\beta \approx 2$ is a calibration coefficient suggested by Wilson (2000).

We then compute the Lagrangian trajectories of the heavy particles based on drag and gravitational forces. We neglect the other terms in the particle momentum equation assuming that particles are small $\left(d_p << \eta\right)$ and heavy $\left(\rho_p/\rho_f >> 1\right)$ (Maxey & Riley, 1983), where η is the Kolmogorov microscale. Indicating the particle position as $X_{p,i}$ and the Lagrangian particle velocity as $U_{p,i}$, we can write

$$\frac{\mathrm{d}X_{p,i}}{\mathrm{d}t} = U_{p,i}, \tag{9}$$

$$\frac{\mathrm{d}U_{p,i}}{\mathrm{d}t} = \frac{\Delta_u}{t_p} - g\delta_{i3}. \tag{10}$$

$\Delta_u = \tilde{u}_i + U_i^{\mathrm{SGS}} - U_{p,i}$ is the difference between the flow velocity and the particle's velocity, where U_i^{SGS} indicates the SGS flow velocity felt by the heavy particle. In equation (10), t_p is the particle relaxation time, which reads

$$t_p = \frac{\rho_p d_p^2}{18\mu} \frac{1}{f\left(\mathrm{Re_p}\right)}, \tag{11}$$

being $\mathrm{Re_p} = |\Delta_u| d_p/\nu$ the particle Reynolds number and $f\left(\mathrm{Re_p}\right) = 1 + 0.15\mathrm{Re_p}^{0.687}$ (Clift et al., 2005).

For particle sizes comparable to or larger than the Kolmogorov microscale η, additional terms should be included in equation (10) to account for velocity gradients across the diameter of the particles (Maxey & Riley, 1983). In the specific case of snowflakes, the analytical formulation of these additional terms is hindered by the complex particle geometry. Nonetheless, corrections to equation (11) that account for the finite size and nonsphericity of particles have been proposed in the literature (e.g., List & Schemenauer, 1971). Particularly relevant for this study is the correction proposed by Loth (2008) for dendritic crystals. Their experimental investigations suggest that these crystals present a much smaller relaxation time, which is well reproduced using $f\left(\mathrm{Re_p}\right) = f_s\left[1 + 0.15\left(\mathrm{Re_p} C_s/f_s\right)^{0.687}\right]$ with $f_s = 3.1$ and $C_s = 25$.

We perform a time integration of equation (10) with a second-order accurate Verlet scheme (Verlet, 1967), which is an explicit integration method often used in molecular dynamics. After updating particle position and velocity, we compute the forcing term $\tilde{F}_i^p$ in equation (1a) as

$$\tilde{F}_i^p\left(\mathbf{x}, t\right) = -\sum_{n=1}^{N_p} f_i^n\left(\mathbf{X}_p^n, t\right) \delta\left(\mathbf{x} - \mathbf{X}_p^n\right), \tag{12}$$

where N_p is the total number of particles, $\delta\left(\mathbf{x} - \mathbf{X}_p^n\right)$ is a Dirac delta function centered on the particle's position, and $f_i^n\left(\mathbf{X}_p^n, t\right)$ is the drag force that the flow exerts on the nth particle, that is,

$$f_i\left(\mathbf{X}_p, t\right) = \frac{\rho_p}{\rho_f} \frac{\Delta_u}{t_p}. \tag{13}$$

Similarly, the particle mass flux reads

$$\tilde{\Phi}_i\left(\mathbf{x}, t\right) = \sum_{n=1}^{N_p} m_p^n U_{p,i}^n\left(\mathbf{X}_p^n, t\right) \delta\left(\mathbf{x} - \mathbf{X}_p^n\right), \tag{14}$$

where m_p^n is the mass of the nth particle. A discrete version of $\delta\left(\mathbf{x} - \mathbf{X}_p^n\right)$ is used in our algorithm, to evaluate the point forces of the particles mass loading (equation (12)), which corresponds to an inverse distance weighting (see, e.g., Richter & Sullivan, 2013). This allows to preserve the integral value of the feedback force while preventing numerical instabilities.

2.4. Dimensionless Formulation

To identify the dependency of flow-particle interactions on the length and velocity scales of interest, we refer to the dimensionless form of the particle transport equations. We can obtain the dimensionless form of the filtered Navier-Stokes equations by normalizing each term of equation (1a) by an appropriate combination of a reference velocity scale U and a reference length scale L, such that

$$\frac{\partial \hat{\tilde{u}}_i}{\partial \hat{t}} + \hat{\tilde{u}}_j\left(\frac{\partial \hat{\tilde{u}}_i}{\partial \hat{x}_j} - \frac{\partial \hat{\tilde{u}}_j}{\partial \hat{x}_i}\right) = -\frac{\partial \hat{\tilde{\pi}}}{\partial \hat{x}_i} - \frac{\partial \hat{\tau}_{ij}^{\mathrm{SGS}}}{\partial \hat{x}_j} - \hat{\Pi}_1 + \hat{\tilde{f}}_i^{\Gamma_s} - \frac{\rho_p}{\rho_f St} \sum_{n=1}^{N_p} \Delta_{\hat{u}}^n \delta\left(\hat{\mathbf{x}} - \hat{\mathbf{X}}_p^n\right). \tag{15}$$

In equation (15), the hat denotes dimensionless variables and

$$St = \frac{t_p U}{L} \tag{16}$$

is the Stokes number. It is worth noting that we focus our interest on highly turbulent atmospheric flows where viscous stresses are generally negligible with respect to turbulent stresses in the bulk of the flow. Further, we are focusing on cases where surface drag is mostly caused by pressure effects (as implicitly

assumed via the usage of equation (2.1e)). For this reason, the Reynolds number does not appear as a control parameter in the normalized LES momentum conservation equation (15).

The dimensionless particle equation of motion reads

$$\frac{\mathrm{d}\hat{U}_{p,i}}{\mathrm{d}\hat{t}} = \frac{\Delta_{\hat{u}}}{St} - \frac{1}{Fr^2}\delta_{i3}, \tag{17}$$

where

$$Fr = \frac{U}{\sqrt{gL}} \tag{18}$$

is the Froude number. Equation (17) suggests that, in neutrally stable atmospheric conditions, the dynamic of small heavy particles depend on two control parameters, that is, the Stokes number and the Froude number. St expresses the ratio between particle inertia and flow advection, while Fr the ratio between particle inertia and gravity. In particular, when $St \to 0$, the first term on the right-hand side of equation (17) becomes dominant and particle dynamics become advection controlled. Conversely, when $Fr \to 0$, the second term becomes dominant and particle dynamics become gravity controlled. In all intermediate conditions, any combination of reference length scale L and velocity scale U yields a unique set of St and Fr and thus a scale-specific deposition process.

It is noteworthy that several previous modeling studies of preferential deposition adopted a form of the advection-diffusion equation that neglects the effect of particle inertia (Lehning et al., 2008; Mott & Lehning, 2010; Mott et al., 2010). We can easily obtain the inertialess form of the particle equation of motion by setting the acceleration term in equation (10) to zero, which yields

$$U_{p,i} = \tilde{u}_i + U_i^{\mathrm{SGS}} - W_s\delta_{i3}. \tag{19}$$

In equation (19), $W_s = gt_p$ denotes the settling velocity of the particles. The dimensionless form of this equation is readily obtained by dividing all terms by the reference velocity scale U, such that

$$\hat{U}_{p,i} = \hat{\tilde{u}}_i + \hat{U}_i^{\mathrm{SGS}} - \hat{W}_s\delta_{i3}, \tag{20}$$

where $\hat{W}_s = W_s/U$ is the dimensionless settling velocity. Equation (20) suggests that the deposition process of inertialess particles depends on the velocity scale U but not on the length scale L.

3. Model Testing

We validate our model against wind tunnel measurements of dust deposition onto isolated hills (Goossens, 2006) and sequential hills (Goossens, 1996). These experimental studies provide us with detailed information on flow field, sediment, and deposition patterns and are thus ideal test cases for the validation of our model. The experiments were conducted in a closed-return wind tunnel of width 120 cm and height 60 cm. The hills were located at the end of a 760-cm-long test section. Upwind of the topography, a turbulent boundary layer developed on a flat rough surface. Dust particles were injected into the air flow using a dust cloud producer. The durations of the experiments were 12 min for the isolated hill and 15 min for the sequential hills. The mass release rate in all experiments was approximately 13 kg/hr. At the end of the experiments, the dust height was determined through scanning of the hill surface (Goossens, 1996) or using an analytical balance (Goossens, 2006). Goossens (2006) and Goossens (1996) indicated that all experiments are Reynolds number independent based on the criterion proposed by Cermak (1984), that is, $u_\tau \bar{h}/\nu > 70$, where u_τ is the friction velocity, $\bar{h}$ the mean elevation of the hills, and ν the kinematic viscosity of air.

In order to minimize the influence of the periodic boundary conditions in the isolated hill simulation (section 3.1), we assign a sufficient domain extension in the x direction, L_x, to recover the boundary layer at the section upwind of the hill. In the sequential hill simulation (section 3.2), the inlet flow is different between the experiment and the simulation because of the periodic boundary conditions. The flow simulation should however be more representative of the experimental flow downwind of the first hill, as the influence of the inlet boundary layer progressively vanishes. In the experiments by Goossens (2006) the wind speed was too low to produce resuspension of deposited dust. We accounted for this by calculating the

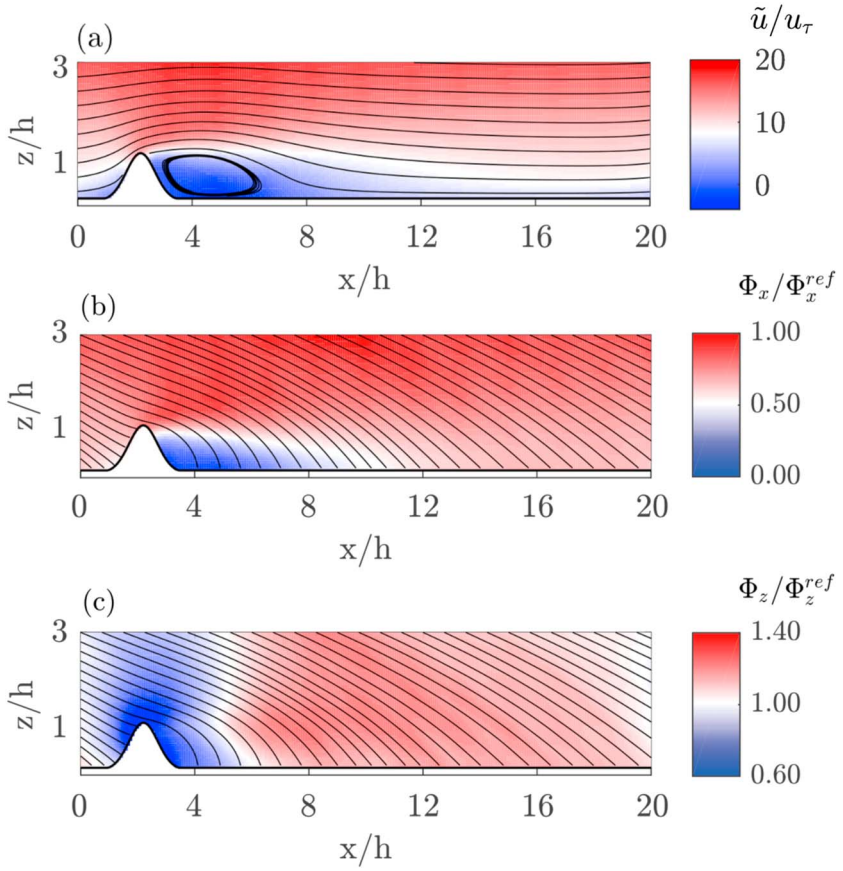

Figure 2. Flow field and mass fluxes over the isolated hill, as provided by the large eddy simulation-Lagrangian stochastic model. (a) Streamlines of the wind field, (b) horizontal mass flux, and (c) vertical mass flux around the Gaussian hill. All quantities are averaged in time and in the y direction. The mass fluxes in (b) and (c) are normalized by reference mass fluxes obtained on flat surface conditions with identical u_τ, particle seeding, domain size, and grid resolution. Solid black lines represent streamlines of wind velocity and mass flux.

deposition pattern assuming that settling particles adhere to the surface. The duration of the simulations is $30T_e$, where T_e is the eddy turnover time.

In our simulations, we release dust particles uniformly from a horizontal plane at elevation $0.8L_z$, where L_z is the height of the computational domain. When particles cross the lateral boundaries, we reinject them from the opposite side of the domain at the same elevation, consistently with the periodic boundary conditions of the flow field.

Since the duration of the experiments was much longer than in our simulations, we compare normalized deposition distributions. Such normalization is necessary because the spatial mean and standard deviation of dust deposition grow in time. At the end of the simulations, we thus compute the normalized dust height distribution $(D-\langle D\rangle)/\sigma_D$, where $\langle D\rangle$ is the spatial mean and σ_D the spatial standard deviation and compare it with that obtained from the experimental results. Note that we adopt this normalization procedure for all deposition patterns presented in this paper. We verified that for simulations longer than $30T_e$ the dust deposition distributions do not show apparent variations.

3.1. Deposition Over Isolated Hill

We design the first simulation of dust deposition over an isolated hill to reproduce the experimental conditions described in Goossens (2006). We consider a Gaussian hill with height $h = 4$ cm, standard deviation $\sigma_h = 2$ cm, and constant profile in the y direction (hill 1 in Goossens, 2006). The boundary layer generated in the fetch of the wind tunnel has free stream velocity $U_\infty = 172$ cm/s, friction velocity $u_\tau = 6$ cm/s, and roughness length $z_0 = 0.001$ cm. The dust particle density is $\rho_p = 2,650$ kg/m^3, and the particle diameter has

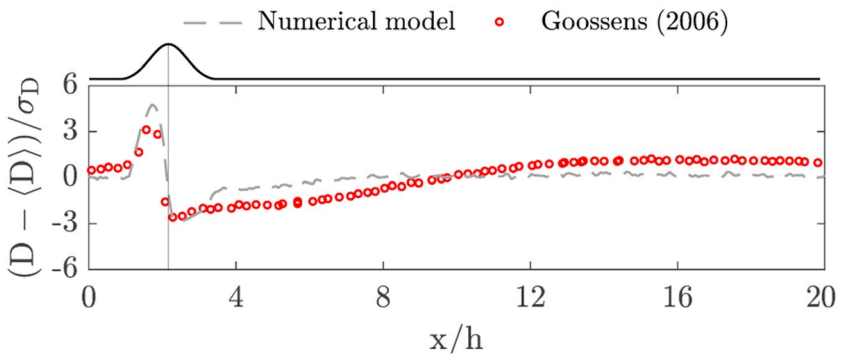

Figure 3. Modeled and measured dust deposition profiles over the isolated hill. The deposition distributions are normalized by the corresponding mean values $\langle D \rangle$ and standard deviations σ_D. The profiles are obtained by averaging the deposition distributions in the y direction.

lognormal distribution with mean $d_p = 50\mu m$, and standard deviation $\sigma_d = 20\mu m$. The particle relaxation time, calculated with equation (11) using the mean particle diameter, is $t_p \approx 0.02$ s.

We define a computational domain with dimensions $L_x = 20$ h, $L_y = 5$ h, and $L_z = 5$ h. The domain is discretized using a Cartesian grid with $N_x = 128$, $N_y = 32$, and $N_z = 49$ nodes, leading to computational cells with dimensions $\Delta_x = \Delta_y = 0.156$ h and $\Delta_z = 0.1$ h. The eddy turnover time is $T_e = 3.3$ s, and the simulation time step is $\Delta_t = 0.01 t_p$. The release rate is 530 particles·m^{-2}·s^{-1}.

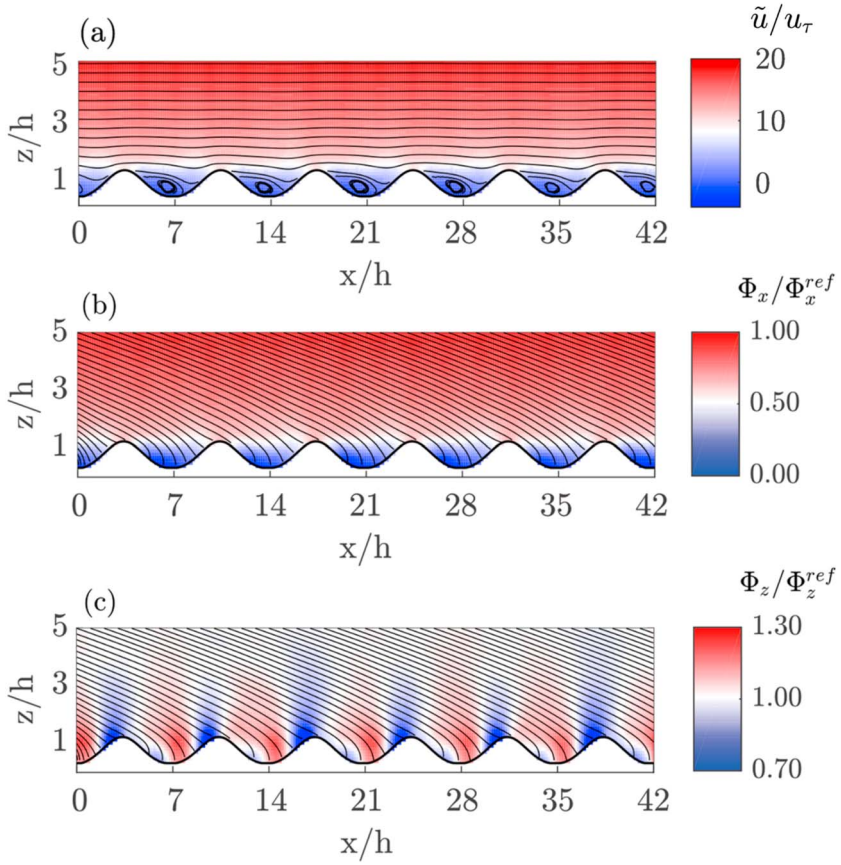

Figure 4. Flow field and mass fluxes over the range of hills, as provided by the large eddy simulation-Lagrangian stochastic model. (a) Streamlines of the wind field, (b) horizontal mass flux, and (c) vertical mass flux around the Gaussian hills. All quantities are averaged in time and in the y direction. The mass fluxes in (b) and (c) are normalized by reference mass fluxes obtained on flat surface conditions with identical u_τ, upper particle seeding, domain size, and grid resolution. Solid black lines represent streamlines of wind velocity and mass flux.

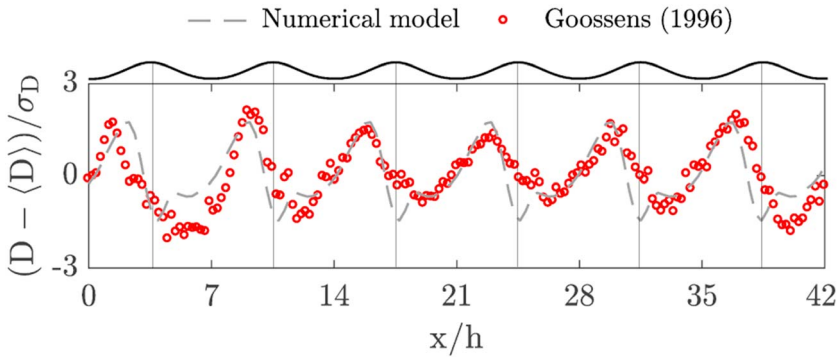

Figure 5. Modeled and measured dust deposition profiles over the sequential hills. The deposition distributions are normalized by the corresponding mean values $\langle D \rangle$ and standard deviations σ_D. The profiles are obtained by averaging the deposition distributions in the y direction.

We show in Figure 2a the time-averaged flow field over the Gaussian hill. The flow accelerates on the windward side of the hilltop, and a wake region extends for a distance of approximately 10 h beyond the hilltop. We also observe an intense and localized updraft region on the windward slope and a wider downdraft region downwind of the hill.

Because mean flow advection plays an important role in the dynamics of dust particles, the time-averaged particle mass flux presents similar features to the mean flow. Figures 2b and 2c show the horizontal and vertical mass fluxes over the Gaussian hill. Note that all figures in this paper represent particle mass fluxes over hills normalized with respect to the corresponding reference mass fluxes over flat surfaces, obtained with equivalent u_τ, upper particle seeding, domain size, and grid resolution. Mass fluxes over hills are thus enhanced with respect to reference mass fluxes on flat terrain in regions where $\Phi_i/\Phi_i^{\mathrm{ref}} > 1$, reduced otherwise. The horizontal particle supply is relatively strong on the windward slope but almost negligible in the wake region (Figure 2b). Furthermore, the wind updraft reduces the downward mass flux around the hilltop by keeping dust particles aloft, while enhancing particle settling in the downdraft region beyond the hill (Figure 2c).

The dust height profiles resulting from the simulation and from the experiment are compared in Figure 3. The model results agree with the measurements on the location and magnitude of deposition maximum and minimum. In particular, we observe an increasing deposition on the windward slope and a local maximum before the hilltop. The dust height then drops rapidly and reaches a local minimum beyond the hilltop. The dust height remains relatively small on the leeward slope and slowly increases toward the mean value in the area below the wake region. We notice that the model predicts a larger deposition below the recirculation region and a slightly smaller dust deposition far downwind of the hill, most likely due to the limited extension of our computational domain in the windward direction in conjunction with the use of periodic boundary conditions.

3.2. Deposition Over Range of Hills

We design the second simulation of dust deposition over a range of hills to reproduce the experimental conditions described in Goossens (1996). Therein, the author investigates dust deposition patterns over ranges of hill with different height and aspect ratios. Here, we consider the case of six consecutive two-dimensional

Table 1
List of Simulations Performed to Study the Sensitivity of the Deposition Process to the Stokes and Froude Numbers

Name	L_x	L_y	L_z	Δ_x	Δ_y	Δ_z	Δ_t	T_e	h	σ_h/h	u_τ	St	Fr
S1	800	200	200	3.13	3.13	2.02	0.01	178	40	0.75	1.00	0.0124	0.0300
S2	400	100	100	1.56	1.56	1.01	0.01	178	20	0.75	0.50	0.0124	0.0150
S3	200	50	50	0.78	0.78	0.51	0.01	178	10	0.75	0.25	0.0124	0.0075
S4	800	200	200	3.13	3.13	2.02	0.01	357	40	0.75	0.50	0.0062	0.0075
S5	3,200	800	800	12.50	12.50	8.08	0.01	713	160	0.75	1.00	0.0031	0.0075

Note. All lengths are given in (m), times in (s), and velocities in (m/s).

Table 2
List of Simulations Performed to Test the Sensitivity of the Deposition Process to the Snowflake Shape

Name	L_x	L_y	L_z	Δ_x	Δ_y	Δ_z	Δ_t	T_e	h	σ_h/h	u_τ	St	Fr
S6	800	200	200	3.13	3.13	2.02	0.01	178	40	0.75	1.00	0.0124	0.0300
S7	200	50	50	0.78	0.78	0.51	0.01	178	10	0.75	0.25	0.0124	0.0075
S8	3,200	800	800	12.50	12.50	8.08	0.01	713	160	0.75	1.00	0.0031	0.0075

Note. All lengths are given in (m), times in (s), and velocities in (m/s).

(y independent) Gaussian hills with height $h = 4$ cm and and standard deviation $\sigma_h = 5.6$ cm. The boundary layer upwind of the topography is characterized by a free stream velocity $U_\infty = 192$ cm/s and friction velocity $u_\tau = 9.3$ cm/s. The dust particles have density $\rho_p = 2,650\ \mathrm{kg/m^3}$, and lognormal diameter distribution with mean $d_p = 30\mu$m and standard deviation $\sigma_d = 7\mu$m. The particle relaxation time, calculated with equation (11) using the mean particle diameter, is $t_p \approx 0.01$ s.

Our computational domain has dimensions $L_x = 42$ h, $L_y = 10.5$ h, and $L_z = 10.5$ h. The Cartesian grid has $N_x = 256$, $N_y = 64$, and $N_z = 99$ nodes, that is, a spatial discretization $\Delta_x = \Delta_y = 0.165$ h and $\Delta_z = 0.105$ h. The eddy turnover time is $T_e = 4.5$ s, and the simulation time step is $\Delta_t = 0.02 t_p$. The particle release rate is approximately 530 particles $\cdot\ \mathrm{m^{-2}} \cdot \mathrm{s^{-1}}$.

We show in Figure 4a the time-averaged flow field over the range of hills. The surface geometry (macroroughness) acts as a displacement height for the boundary layer, which recovers horizontal homogeneity at $z \approx 3$ h (roughness sublayer height). The flow field within the interfacial layer, defined as the layer below the hill height, presents a weak wake zone that is limited in extension by the interhill distance.

Figures 4b and 4c show the horizontal and vertical mass fluxes over the range of hills, normalized with respect to the reference mass fluxes over flat terrain. The particle mass flux reflects some of the features of the flow field. As experimentally observed by Goossens (1996), the horizontal particle supply to the valleys is almost negligible (Figure 4b) as most of the mass flux is provided vertically by the flow downdrafts (Figure 4c).

Figure 5 shows the comparison between the modeled and the measured dust height profiles at the surface. We notice that the differences between model results and experiments are larger over the first hill, where the LES is less representative of the experimental flow due to the periodic boundary conditions. The results are however in good agreement downwind of the first hill, where the LES provides a more accurate description of the experimental flow. In particular, model and experiments indicate a relatively large deposition on the windward slopes, with local maximum before the hilltops, a rapid drop corresponding to each hilltop and a small deposition on the leeward slopes. The cross comparison between Figures 4 and 5 suggests that the increase of deposition at the toes of the windward slopes is mainly due to the flow downdrafts, while the local maxima before the hilltops are mainly due to horizontal mass flux supply.

It is worth noting that the simulation indicates the presence of a dip and increase in deposition on the leeward slopes, which is not clearly visible in the experiments. From a cross comparison of Figures 4 and 5, we notice that the locations of the dips correspond to the locations where the particle mass flux is approximately parallel to the hill surface, that is, where the flux normal to the surface is minimum. The reason for the presence of this dip in our simulations could thus lie in a slight overestimation of the horizontal component of the mass flux with respect to the experiments.

Table 3
List of Simulations for Inertialess Particles With Corresponding Domain Size, Spatial and Temporal Resolutions, and Dimensionless Settling Velocity

Name	L_x	L_y	L_z	Δ_x	Δ_y	Δ_z	Δ_t	T_e	h	σ_h/h	u_τ	$\hat{W}_s$
S9	800	200	200	3.13	3.13	2.02	0.01	178	40	0.75	1.00	0.08
S10	200	50	50	0.78	0.78	0.51	0.01	178	10	0.75	0.25	0.33
S11	3,200	800	800	12.50	12.50	8.08	0.01	713	160	0.75	1.00	0.08

Note. All lengths are given in (m), times in (s), and velocities in (m/s).

Table 4
List of Simulations Performed to Study the Sensitivity of the Deposition Process to the Hill Aspect Ratio

Name	L_x	L_y	L_z	Δ_x	Δ_y	Δ_z	Δ_t	T_e	h	σ_h/h	u_τ	St	Fr
S12	800	200	200	3.13	3.13	2.02	0.01	178	40	0.375	1.00	0.0124	0.0300
S13	200	50	50	0.78	0.78	0.51	0.01	178	10	0.375	0.25	0.0124	0.0075
S14	3,200	800	800	12.50	12.50	8.08	0.01	713	160	0.375	1.00	0.0031	0.0075

Note. All lengths are given in (m), times in (s), and velocities in (m/s).

Although small differences between simulations and measurements are visible, our model provides reliable simulations of dust deposition on both isolated and sequential hills. Although a direct validation for snow particle deposition is impaired by the lack of experimental data, we feel confident to use the model to perform snowfall simulations given that particle shape, dimension, and density are explicitly accounted for in the transport equations.

4. Simulation Setup for the Sensitivity Analysis

We perform a series of snowfall simulations over a Gaussian hill, adopting different combinations of U and L to test the sensitivity of snowfall deposition to the Stokes and Froude numbers. Specifically, we define $L \equiv h$ and $U \equiv u_\tau$, where h is the height of the Gaussian hill and $u_\tau \approx \sqrt{\Pi_1 L_z}$ is the friction velocity, which includes both the hill pressure drag and the skin friction drag. The Gaussian hill has standard deviation $\sigma_h = 0.75$ h and a constant profile in the y direction. We locate the hill in a regular computational domain of dimension $L_x = 20$ h and $L_y = L_z = 5$ h. Even though the flow boundary conditions are periodic, the length of domain in the x direction is sufficient to have an approximately undisturbed flow field upwind of the hill (Grimmond & Oke, 1999). We define the grid resolution based on the resolution analysis presented in Appendix A, which indicates that a Cartesian grid with $N_x = 256$, $N_y = 64$, and $N_z = 99$ nodes in the x, y, and z directions is sufficient to simulate snowfall deposition patterns at the scales of interest.

Snowflakes present remarkable differences in shape depending on temperature and humidity upon formation (Nakaya, 1954). We can account for some of the effects of aspherical geometries by assuming spherical

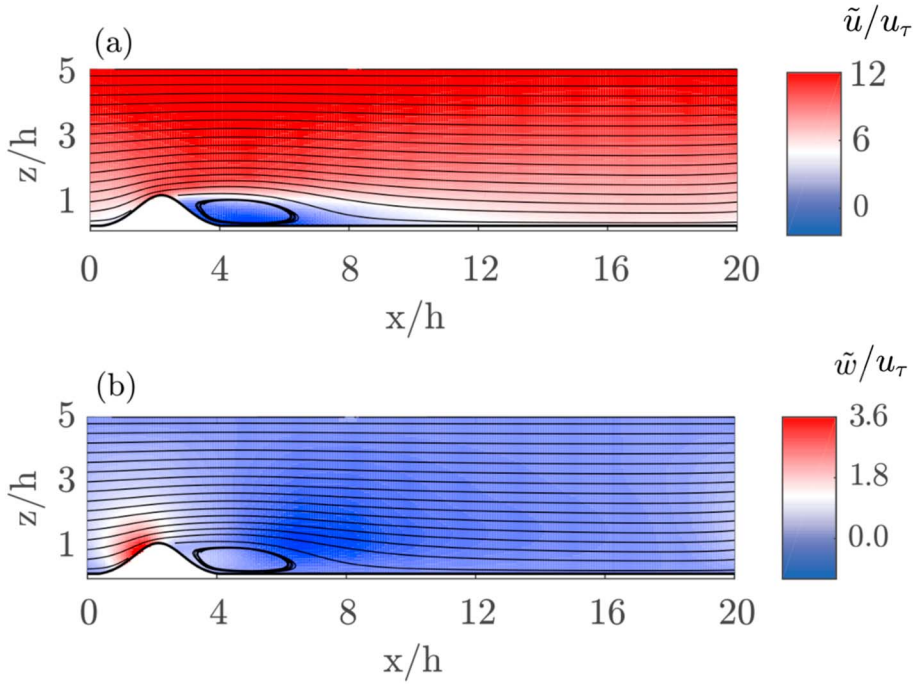

Figure 6. Large eddy simulation flow field over the Gaussian hill. (a) Horizontal flow velocity and (b) vertical flow velocity. All quantities are averaged in time and in the y direction. Solid black lines represent streamlines of wind velocity.

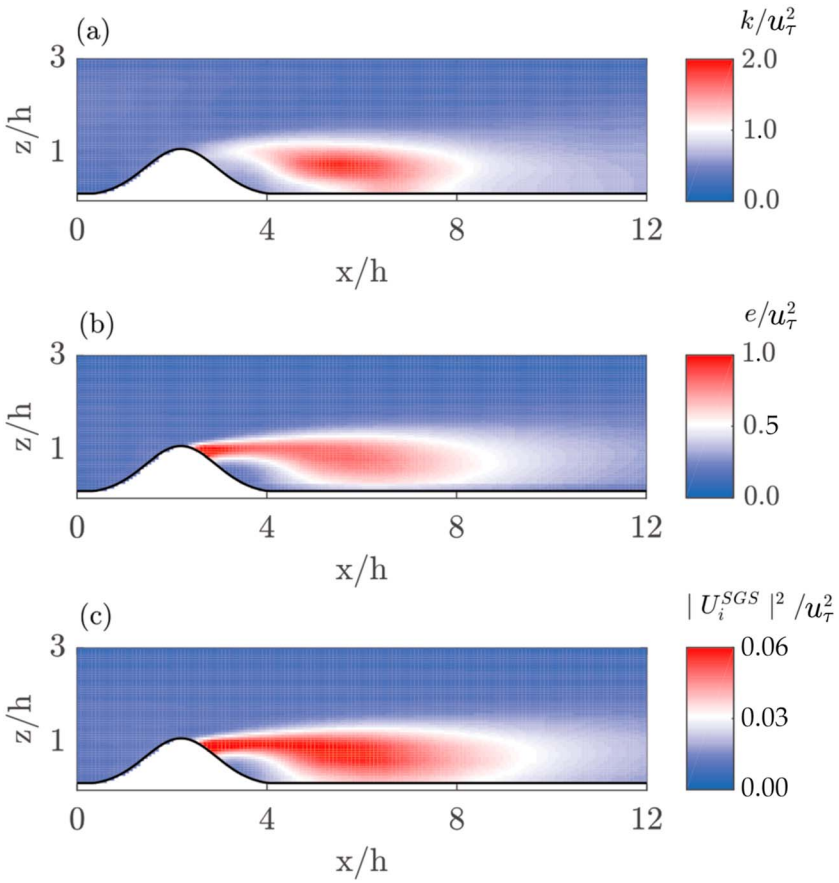

Figure 7. (a) Turbulent kinetic energy of the large eddy simulation-resolved flow field (see equation (7)), (b) time-averaged subgrid scale turbulent kinetic energy (see equation (5)), and (c) subgrid scale flow fluctuations as predicted by the Lagrangian stochastic model (see equation (4)). All variables are averaged in time and in the y direction.

particles with an equivalent diameter, here $d_p = 2$ mm and reducing the effective particle density ρ_p. Magono (1965) and Passarelli and Srivastava (1979) collected a large number of natural snowflakes and observed that their effective density approximately decays with the square of their effective diameter. According to their studies, the equivalent density of snowflakes with effective diameter $d_p = 2$ mm is approximately $\rho_p = 500$ kg/m^3, yielding a particle relaxation time $t_p \approx 0.5$ s.

We release snowfall particles from a horizontal plane at elevation $0.8\,L_z$. The precipitation has intensity of 10 mm/hr, corresponding to a particle release rate of 83 particles $\cdot$ m^{-2} $\cdot$ s^{-1}, constant in time and uniform over the plane of release. If snow particles cross the lateral boundaries, they are relocated in the opposite side of the domain at the same elevation. We calculate the deposition pattern assuming that settling particles adhere to the surface. We assume that the aerodynamic roughness is typical of a snow surface, that is, $z_0 = 0.1$ mm (Kikuchi, 1981).

It is worth noting that large snowflakes are likely to break into smaller fragments upon impact with the surface (Comola et al., 2017; Sato et al., 2008). These smaller particles are then easily lifted from the surface through aerodynamic entrainment and granular splash (e.g., Comola & Lehning, 2017; Diplas et al., 2008), which lead to drifting snow events. Because the focus of this study is snowfall deposition, we do not account for drifting snow in our simulations. The separation of snowfall from drifting snow, albeit artificial, allows us to single out the role played by preferential deposition in the snow height spatial variability.

We list in Table 1 the series of simulations performed to test the sensitivity of the deposition process to the Stokes and Froude numbers. The progression S1 → S2 → S3 is characterized by a constant Stokes number and a decreasing Froude number, that is, an increasing effect of gravity on particle dynamics. Conversely, the

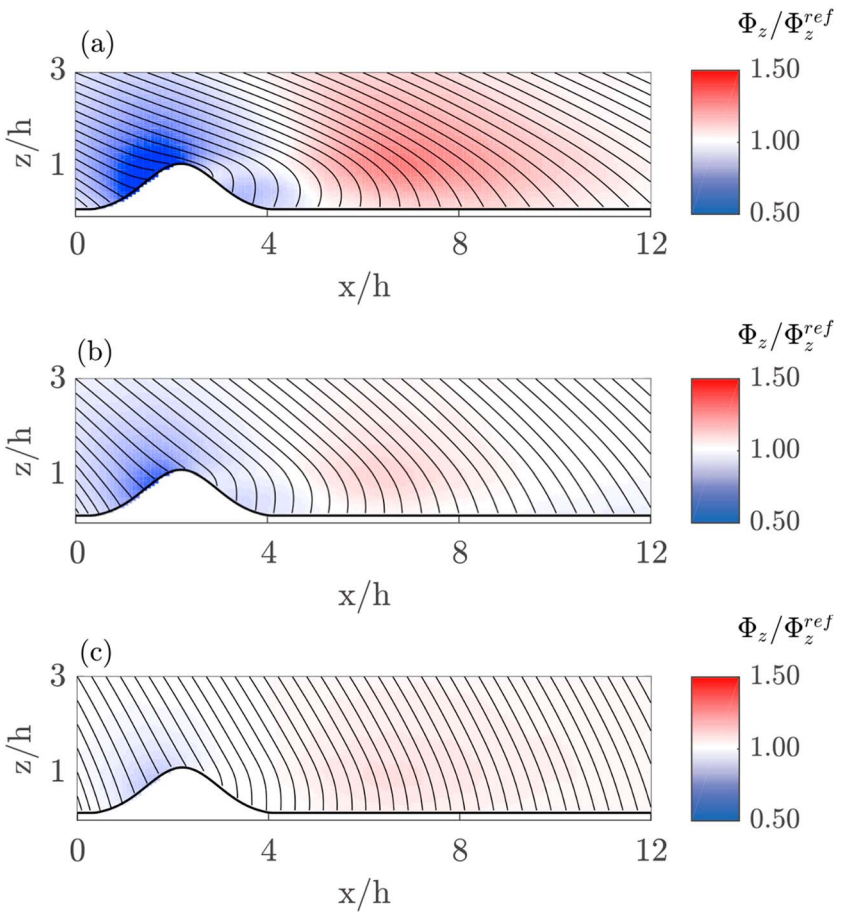

Figure 8. Evolution of the vertical mass flux around the Gaussian hill for decreasing values of Froude number. (a) Simulation S1 ($St = 0.0124$, $Fr = 0.0300$), (b) simulation S2 ($St = 0.0124$, $Fr = 0.0150$), and (c) simulation S3 ($St = 0.0124$, $Fr = 0.0075$). The fluxes are averaged in the y direction and normalized by the reference mass flux obtained on flat surface conditions with identical u_τ, particle seeding, domain size, and grid resolution. Solid black lines represent streamlines of mass fluxes.

progression S3 → S4 → S5 is characterized by a constant Froude number and a decreasing Stokes number, that is, a growing control of flow advection on particle dynamics.

A second series of model simulations (S6, S7, and S8), listed in Table 2, carried out with a reduced relaxation time that best represents the dynamics of dendritic crystals (Loth, 2008). In terms of hill size and flow velocity, simulation S6 is equivalent to simulation S1, S7 is equivalent to S3, and S8 is equivalent to S5. This analysis will clarify whether the assumption of small, spherical particles holds for snowflakes of finite size and irregular shape. Adopting an equivalent diameter $d_p = 2$ mm, $\rho_p = 910$ kg/m^3 (ice density), $f_s = 3.1$, and $C_s = 25$ in equation (11), we obtain a reduced particle relaxation time $t_p \approx 0.05$ s.

The third series of model runs (simulations S9, S10, and S11 listed in Table 3) are performed with the inertialess version of the particle equation of motion (equation (19)). We aim at investigating if the approximation of inertialess snowflakes, adopted in most previous studies on preferential deposition (Lehning et al., 2008; Mott & Lehning, 2010; Mott et al., 2010), can provide effective simulations of the deposition process. In particular, simulation S9 presents the same length and velocity scales as simulation S1, simulation S10 the same as S3, and simulation S11 the same as S5. We adopt a settling velocity $W_s = 1$ m/s, which corresponds to the mean value observed in recent field investigations (Garrett & Yuter, 2014).

The fourth series of simulations, listed in Table 4, aims at highlighting the effect of the hill aspect ratio on the deposition process. The hill steepness, in fact, may significantly affect the near-surface flow field and thus the control of flow advection on particle dynamics. We thus perform three simulations (S12, S13, and

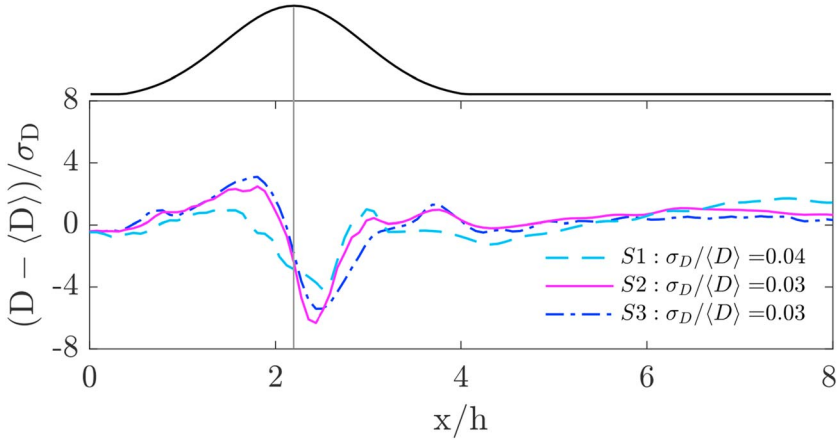

Figure 9. Snow height profiles, averaged in the y direction, for decreasing values of Froude number (see Table 1 for more details). The plots show the deposited snow height D, normalized with respect to the spatial mean $\langle D \rangle$ and spatial standard deviation σ_D. The profiles are averaged in the y direction.

S14) that have the same h and u_τ of simulations S1, S3, and S5 but a steeper hill with standard deviation $\sigma_h = 0.375$ h.

All simulations have a duration of $6T_e$. At the end of each simulation, we compute the snow height distribution by subtracting to the height in each surface node D the spatial mean $\langle D \rangle$ and dividing by the spatial standard deviation σ_D. We verified that for simulations longer than $6T_e$ the snow deposition distributions do not show visible variations.

5. Results

5.1. Flow Field

We show in Figure 6 the LES-resolved flow field around the Gaussian hill in absence of airborne particles, normalizing velocities and lengths with respect to u_τ and h, respectively. Figure 6a indicates that a wake region extends for a distance of 6 h beyond the hilltop and that the undisturbed flow field is visually recovered at a distance 12 h from the hill. The vertical flow velocity, shown in Figure 6b, presents a strong updraft at the windward side of the hill and an extended downdraft region between 3 and 10 h beyond the hill. The modeled flow field around the hill and in particular the extension of the wake region are in good agreement with the wind tunnel studies by Simoëns et al. (2015), carried out in flow regimes that satisfy the criterion for Reynolds number independence proposed by Cermak (1984).

Figures 7a and 7b show the spatial variation of resolved turbulence kinetic energy k, (equation (7)) and subgrid turbulence kinetic energy e (equation (5)). Figure 7a shows that the largest fraction of resolved turbulence kinetic energy k is produced in the shear layer that separates from the hill, as was also observed in previous experimental and model studies (Kim et al., 1997), while the largest fraction of the subgrid turbulence kinetic energy e is maximum just beyond the hilltop where the flow shear is largest (Figure 7b). This is also the region where we observe the largest subgrid scale turbulent fluctuations (U_i^{SGS}), as indicated in Figure 7c. Equation (4), in fact, suggests that U_i^{SGS} is larger where the SGS fraction of the total turbulent kinetic energy is large, that is, where $\alpha = e/(e+k)$ approaches unity.

5.2. Sensitivity of Preferential Deposition to the Froude Number

Here, we present our model results for decreasing values of the Froude number, that is, for a deposition process that progressively becomes gravity controlled. Figure 8 shows the spatial variation of the vertical mass flux and the direction of the mass flux (black arrows) for decreasing values of the Froude number. The model results highlight that the direction of the mass flux progressively turns downward as the Froude number decreases (simulations S1 → S3). In fact, the snowfall direction is significantly affected by flow updrafts and downdrafts when the Froude number is large (Figure 8a). Conversely, for the smallest Froude number (Figure 8c), the snowfall direction is predominantly vertical and weakly affected by the near-surface flow. In fact, as gravity forces particle trajectories to align along the vertical direction, the vertical mass flux tends to become spatially homogeneous.

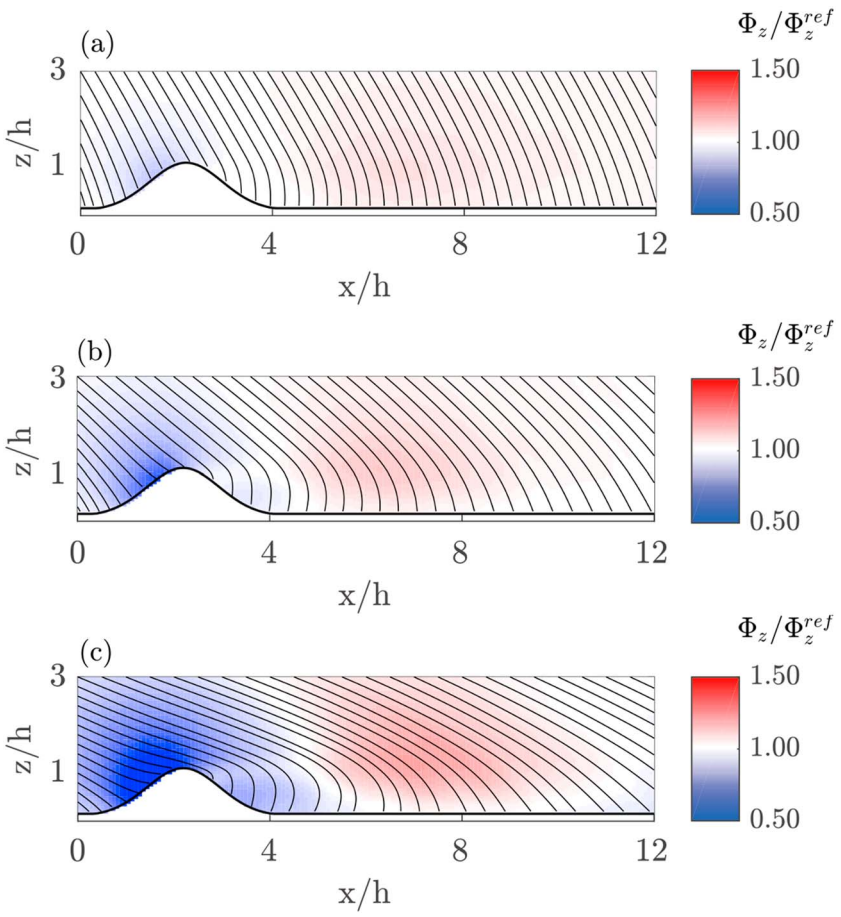

Figure 10. Evolution of the vertical mass flux around the Gaussian hill for decreasing values of Stokes number. (a) Simulation S3 ($St = 0.0124$, $Fr = 0.0075$), (b) simulation S4 ($St = 0.0062$, $Fr = 0.0075$), and (c) simulation S5 ($St = 0.0031$, $Fr = 0.0075$). The fluxes are averaged in the y direction and normalized by the reference mass flux obtained on flat surface conditions with identical u_*, particle seeding, domain size, and grid resolution. Solid black lines represent streamlines of mass fluxes.

The snow height profiles (Figure 9) indicate that, for the largest values of Fr (simulation S1), the deposition pattern is characterized by a relatively small local maximum on the windward slope, a local minimum on the hilltop, and a second large local maximum on the leeward slope. Moreover, a significant amount of snow deposits on the flat terrain beyond the hill. The locations of the deposition maxima well correspond to the areas of strong downward mass flux seen in Figure 8a. As the Froude number decreases and particle dynamics become gravity controlled (simulation S3), the local deposition maximum on the windward slope increases and the local maximum on the leeward slope decreases. We also notice the formation of a second local maximum at the toe of the leeward slope. Furthermore, the deposition maximum below the wake zone progressively disappears.

The reason for the increased deposition on the windward slope lies in the reduced sensitivity of the gravity-controlled process to the flow updraft, as shown in Figure 8c. As a consequence, fewer particles reach the sheltered lee side of the hill and the deposition maximum on the leeward slope decreases. The small sensitivity of the particle mass flux to the flow downdraft in the wake region (Figure 8d) also explains the reduction in snowfall deposition on the flat terrain beyond the hill.

Because the Stokes number is constant, the effect of flow advection on particle acceleration in the x direction is preserved. Accordingly, the locations of deposition maxima and minima are approximately constant across the simulations, as shown in Figure 9.

5.3. Sensitivity of Preferential Deposition to the Stokes Number

As anticipated in section 2.4, a decrease in the Stokes number leads to a larger control of flow advection on particle dynamics. Figure 10 shows the spatial variations in the vertical mass flux and the direction of the

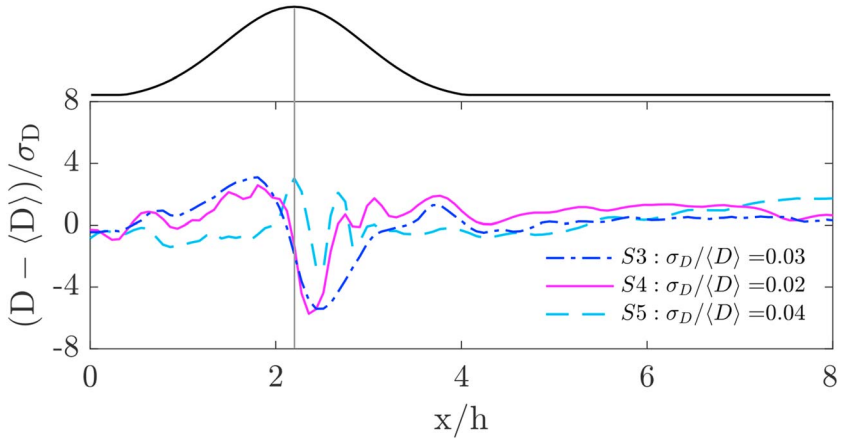

Figure 11. Snow height profiles, averaged in the y direction, for decreasing values of Stokes number (see Table 1 for more details). The plots show the deposited snow height D, normalized with respect to the spatial mean $\langle D \rangle$ and spatial standard deviation σ_D. The profiles are averaged in the y direction.

mass flux (black arrows) across simulations S3 → S5. The results indicate that the direction of the particle mass flux changes according to the near-surface flow field when the Stokes number decreases (Figures 10a to 10c). In particular, flow advection intensifies the horizontal component of the mass flux with respect to the vertical one. Furthermore, the flow updraft effectively reduces particle settling on the windward slope, while the flow downdraft beyond the hill enhances particle deposition. With respect to the gravity-controlled deposition (simulation S3), the vertical mass of the advection-controlled process presents a spatial variability that is well correlated to that of the vertical wind velocity.

Figure 11 shows the snow height profiles obtained from simulations S3 → S5. We notice that the snow height on the windward slope decreases with decreasing Stokes number, as the flow updraft effectively keeps particles aloft. Figure 11 highlights that a decrease in the Stokes number is associated to a downwind displacement of the deposition maximum on the windward slope. Moreover, we observe the formation of a second local maximum on the leeward slope, just beyond the flow separation point. Furthermore, the results indicate a remarkable difference in snow height on the flat terrain beyond the hill, where the much larger deposition occurs in the case of small Stokes number due to the flow downdraft (see Figure 6b for a pseudo color plot of the vertical velocity field).

Similar to what was observed in section 5.2, a decrease in the deposition maximum on the windward slope is compensated by an increase of deposition on the leeward slope. As the flow updraft effectively keeps particles aloft, more and more snowflakes are caught in the separated flow region and eventually settle on the leeward slope. The location of the deposition maxima and minima, however, is not preserved across simulations S3 → S5. Variations in the Stokes number affect the response of particle dynamics to flow acceleration in both horizontal and vertical directions. This leads to the visible downwind displacement of the deposition maximum on the windward slope and the upwind displacement of the deposition maximum on the leeward slope, as flow recirculation advects particles uphill.

5.4. Deposition of Dendritic Crystals and Inertialess Particles

Figures 12a–12c show the deposition patterns of inertial spherical particles (dash-dotted blue lines), inertial dendritic crystals (solid magenta lines), and inertialess particles (dashed cyan lines) for the three different combinations of h and u_τ listed in Tables 2 and 3.

The results suggest that the snowflake shape and the particle inertia significantly affect the deposition pattern for all the tested length and velocity scales. In particular, when the reference velocity scale is large (Figures 12a and 12c), the deposition pattern of dendritic crystals presents a remarkable deposition maximum beyond the hilltop, almost reversing the pattern of spherical particles. Interestingly, we also observe such deposition maximum in the deposition profile of inertialess particles. On the other hand, when the reference velocity scale is small (Figure 12b), the deposition patterns of dendritic crystals and inertialess particles seem to be reasonably close to that of spherical particles, although some differences are visible around to the hilltop. Specifically, dendritic crystals yield a smaller deposition on the windward slope, a local

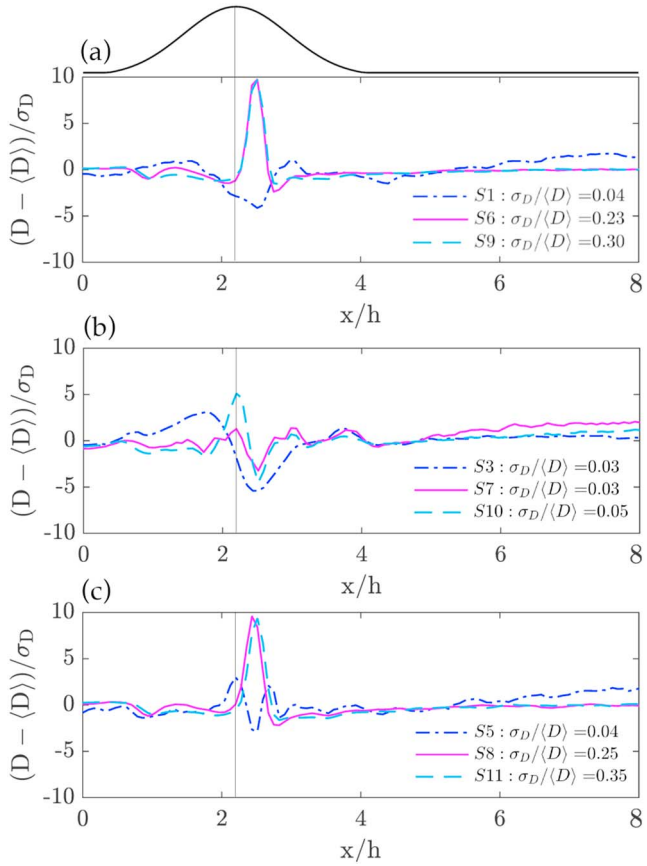

Figure 12. (a–c) Results of the snow deposition simulations assuming dendritic crystals and inertialess particles, as listed in Tables 2 and 3. The plots show the deposited snow height D, normalized with respect to the spatial mean $\langle D \rangle$ and spatial standard deviation σ_D. The profiles are averaged in the y direction.

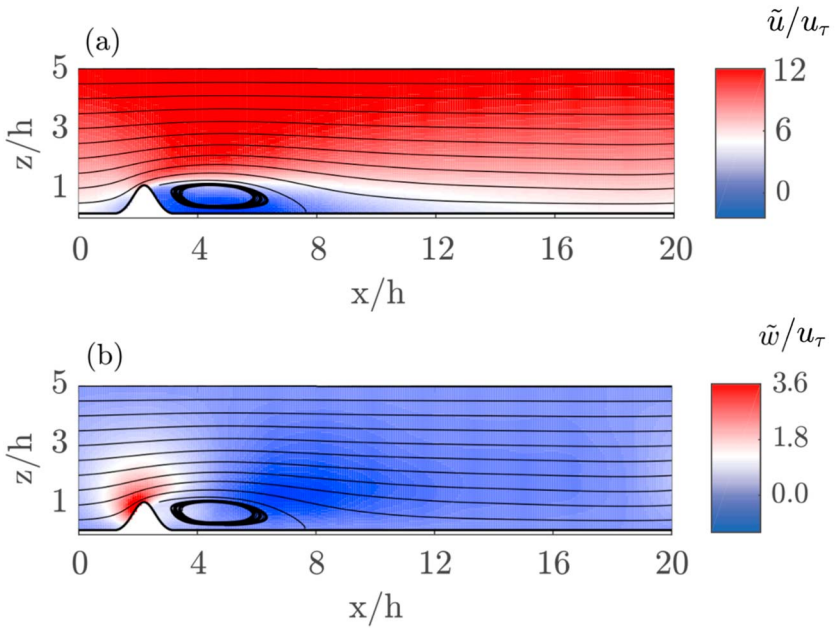

Figure 13. Time-averaged large eddy simulation flow field over the steeper Gaussian hill. (a) Horizontal flow velocity and (b) vertical flow velocity. The flow field is averaged in the y direction. Solid black lines represent streamlines of wind velocity.

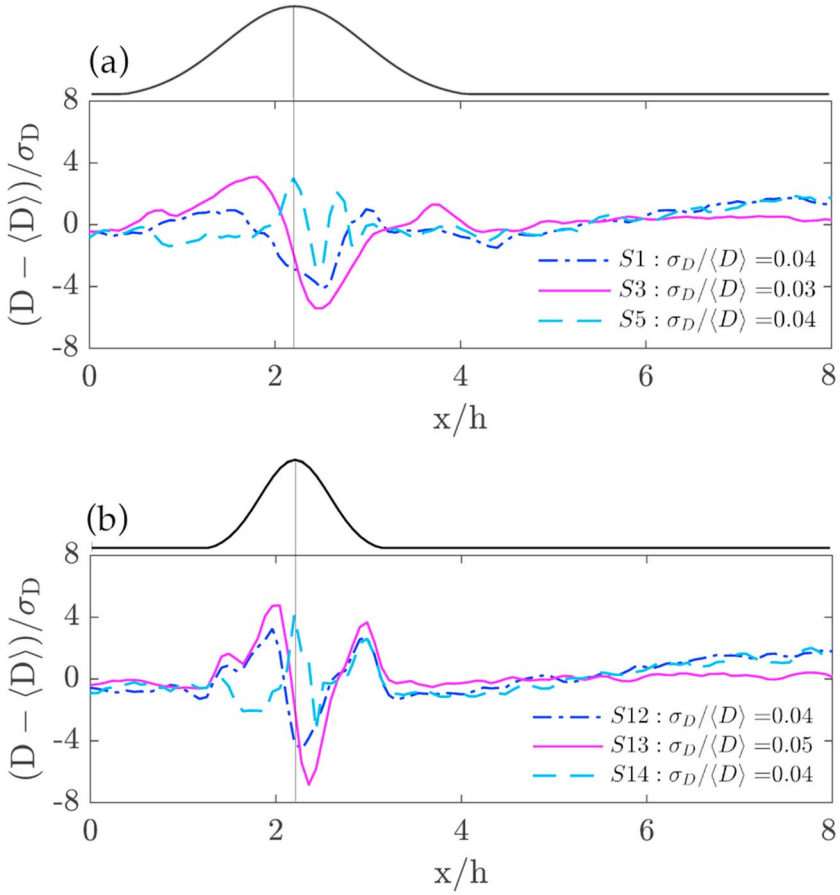

Figure 14. Results of the snow deposition simulations for the two different hill aspect ratios. (a) Deposition profiles for simulations S1, S3, and S5 (see Table 1). (b) Deposition profiles for simulations S12, S13, and S14 (see Table 4). The plots show the deposited snow height D, normalized with respect to the spatial mean $\langle D \rangle$ and spatial standard deviation σ_D. The profiles are averaged in the y direction.

maximum on the hilltop, and a larger deposition on the leeward slope. The snow accumulation around the hilltop becomes even larger and more localized when assuming inertialess particles.

5.5. Sensitivity of Preferential Deposition to the Hill Aspect Ratio

We show in Figure 13 the LES-resolved flow field around the steeper Gaussian hill, obtained with a lower variance of the surface-generating Gaussian function. Figure 13a shows the near-surface flow in the x direction and indicates that the wake region extends for a slightly longer distance compared to the reference hill (Figure 6a). Moreover, the steeper hill seems to produce a longer wake region. The vertical flow velocity, shown in Figure 13b, is characterized by a more intense updraft that extends further downwind from the hilltop compared to the reference hill (Figure 6b). The downdraft region also extends further downwind compared to the reference hill.

Figure 14 compares the deposition patterns over the reference hill (a) and the steeper hill (b) for different combinations of Stokes and Froude numbers. Overall, our results suggest that the general trend observed for the reference hill is preserved in the deposition profiles of the steeper hill. In particular, for larger Stokes and Froude numbers (simulation S12) the deposition profile presents a deposition maximum on the windward slope, a remarkable minimum and a subsequent maximum on the leeward slope, and a large deposition below the downdraft regions. For large Stokes number and small Froude number (simulation S13), there is an increase of the deposition maximum on the windward slope, a decrease of the deposition minimum on the leeward slope, and a flattening of the deposition profile downwind of the hill. For small Stokes and Froude numbers (simulation S14), the windward slope deposition drops, the deposition maximum moves downwind toward the hilltop, and the overall deposition increases on the leeward side and below the recirculation region.

Interestingly, for the steeper hill case we observe the formation of persistent local maxima at the toes of the hillslopes, particularly the leeward slope, probably due to an increased flow blocking.

6. Discussion and Conclusions

The preferential deposition of heavy particles on complex terrain is relevant to a variety of environmental processes, such as the cycles of snow accumulation and melting in alpine regions and the supply of dustborne nutrients to ecosystems over landforms. We aimed at unraveling the governing processes and the relevant scales of heavy particle deposition over hills. Specifically, we carried out model simulations to investigate how different deposition patterns emerge from different combinations of hill size h, the reference length scale, friction velocity u_τ, and the reference velocity scale. Each combination is characterized by a specific set of Froude and Stokes number and thus by a specific interaction among particle inertia, flow advection, and gravity.

The model results suggest that the combination of Stokes and Froude numbers significantly affects the snowflake deposition process. In particular, gravity dominates particle dynamics when the Froude number decreases. On the other hand, flow advection dominates the deposition process when the Stokes number decreases. Model results indicate that, when particle dynamics are gravity dominated, snowflake deposition becomes less sensitive to the near-surface flow. The resulting deposition pattern is characterized by a relatively large snow height on the windward slope, an upwind displacement of the local maximum, and a flattening of the local maximum on the leeward slope. These results are consistent with those obtained by Salesky et al. (2019), who used an Eulerian framework to simulate deposition of heavy particles in similar topographic and atmospheric conditions.

Conversely, when snowfall deposition is advection dominated, particle inertia plays a limited role and snowflakes are easily accelerated upward and downward by the near-surface flow. We showed that the resulting snow height distribution is consistent with the preferential deposition pattern initially described by Lehning et al. (2008), with a relatively small deposition on the windward slope, a local maximum on the hilltop, and a second one on the leeward slope. Moreover, our model results support and extend previous findings by Wang and Huang (2017), who observed that the deposition on the leeward slope increases with increasing flow advection. Even though our analysis focused on the effect of mean flow advection on preferential deposition, turbulence significantly enhances particle mixing both at large and small scales. Turbulence-driven mixing is likely to play a fundamental role in simulations of seeder-feeder and orographic precipitation, where particle release above the topography is not well mixed but rather localized in intense source areas.

In light of our scale analysis, we can interpret the results of the dust deposition experiments (section 3). Both experiments present Froude and Stokes numbers much larger than those tested in the snowfall analysis, $Fr^2 = 4.38$, $St = 0.86$ for the deposition on the single hill and $Fr^2 = 4.89$, $St = 0.48$ for that on the range of hills. The effects of both gravity and flow advection on the dynamics of dust particles around the hill are thus small compared to the snowfall case. Consequently, particles maintain their inertial trajectories and settle on the windward slope causing the local deposition maximum. The small deposition on the leeward slope and on the flat terrain beyond the hill, or in the valleys in case of range of hills, is due to the small effect of advection in the wake and downdraft regions. We thus refer to this type of deposition process as inertia controlled.

Our results further highlight the significant sensitivity of the deposition pattern to the shape of the snowflakes, as dendritic crystals can fully reverse the deposition pattern with respect to rounded snow particles. Dendritic crystals tend to follow the flow trajectories more closely than rounded grains because of their smaller Stokes number. Interestingly, there seems to be a good agreement between the deposition pattern of dendritic crystals and that of inertialess particles, particularly in case of large friction velocity. This suggests that the assumption of inertialess particles, used in several previous studies of preferential deposition (Lehning et al., 2008; Mott & Lehning, 2010; Mott et al., 2010), may provide effective simulations of snowfall deposition for dendritic crystals in high speed flows. For more rounded shapes, however, neglecting particle inertia may lead to large errors in the snow height distribution. Note that because LES models only resolve the energy-containing scales of turbulence, our simulations do not account for small-scale anisotropic interactions between the flow and aspherical particles. Consequently, some aspects of snowfall deposition may

be misrepresented. For instance, snowflakes may present preferential orientations and lower sedimentation rates in the shear layer, whereas their orientation may be randomized and their sedimentation rate closer to the isotropic average in the recirculation zone (Voth & Soldati, 2017).

We finally showed that the results of our scale analysis are qualitatively similar for hills with different aspect rations σ_h/h. It is worth noting that our simulations highlighted an increased deposition at the toe of the slopes of the steeper hill, which is sometimes observed in nature as a result of flow blocking in front of extremely steep slopes. It is also possible that a much larger deposition at the toe of windward slope may form in condition of stable atmospheric stratification. It would be interesting to quantify the impact of atmospheric stability in future studies of snowfall deposition, for example, by including the Brunt-Väisälä frequency in the definition of the Froude number (Dadic et al., 2013).

Further work is also necessary to investigate the influence of drifting snow on the spatial variability of snow depth. A comprehensive study on the combined effect of snowfall deposition and drifting snow may ultimately lead to a deeper insight on the dynamics leading to the formation of snow surface features, such as snow dunes, sastrugi, and snow cornices.

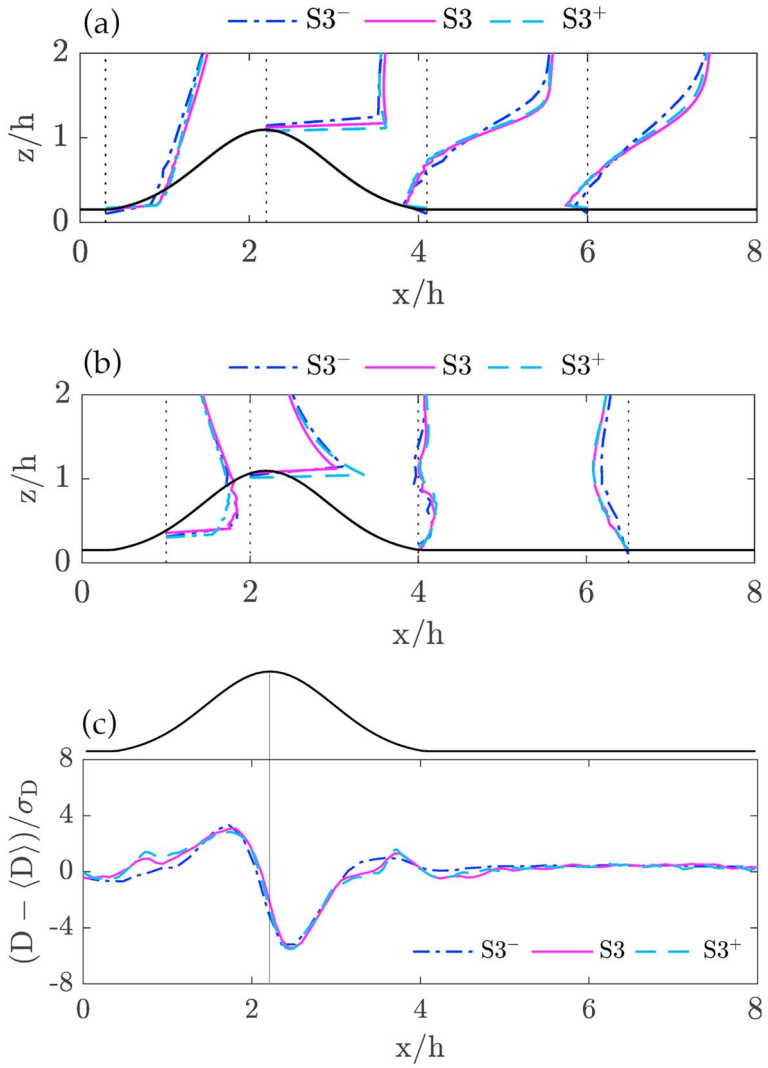

Figure A1. Results of the grid resolution analysis. S3 indicates the reference simulation (see Table 1) with $N_x = 256$, $N_y = 64$, and $N_z = 99$ grid points in the x, y, and z directions. S3$^-$ indicates the coarser numerical grid with $N_x = 128$, $N_y = 32$, and $N_z = 49$ and S3$^+$ the finer grid with $N_x = 384$, $N_y = 96$, and $N_z = 149$. (a) Vertical profiles of streamwise velocity $\tilde{u}$. (b) Profiles of vertical velocity $\tilde{w}$. (c) The deposition profiles. Velocity profiles show the flow field averaged in time and in the y direction.

In conclusion, we have attempted a comprehensive exploration of the main factors influencing heavy particle deposition over hills, that is, the Stokes and Froude numbers, particle shape and inertia, and hill aspect ratio. Our analyses indicate that the deposition patterns of dust and snow over hills present deposition maxima located either on the windward or the leeward side depending on the scales of interest and particle properties. Moreover, our investigation clearly identified the effect of each parameter and provided useful benchmarks to evaluate what deposition pattern should be expected in real world cases, given certain hill height h, friction velocity u_τ, and particle geometry.

Appendix A: Grid Resolution Analysis

We present here the results of the grid resolution analysis that we performed to assign the appropriate number of grid points to the LES simulations presented in section 4. For this purpose, we selected simulation S3 as a test case (see Table 1). In addition to the reference resolution $N_x = 256$, $N_y = 64$, and $N_z = 99$, we test a coarser grid with $N_x = 128$, $N_y = 32$, and $N_z = 49$ (simulation S3$^-$) and a finer grid with $N_x = 384$, $N_y = 96$, and $N_z = 149$ (simulation S3$^+$). The duration of the simulations is $6T_e$, and the time step is $\Delta_t = 0.02t_p$.

We show in Figure A1 the comparison between the vertical profiles of the time-averaged streamwise velocity $\tilde{u}$ (Figure A1a) and time-averaged vertical velocity $\tilde{w}$ (Figure A1b) in relevant sections of the computational domain, that is, in correspondence of local maxima and minima (the entire flow field is represented in Figure 6 for reference). Overall, all three simulations provide similar and consistent results, although there are some visible differences. Specifically, Figure A1a indicates that simulation S3$^-$ is affected by a velocity deficit with respect to simulations S3 and S3$^+$, both in the speedup and in the recirculation zones. Moreover, Figure A1b suggests that simulation S3$^-$ slightly underestimates the updraft and downdraft with respect to simulations S3 and S3$^+$. These differences in the mean flow result in small yet visible variations in the deposition pattern shown in Figure A1c. In particular, simulation S3$^-$ leads to slightly smaller deposition on the windward slope and larger deposition on the leeward slope.

Small differences are also visible between simulations S3 and S3$^+$. Figure A1b indicates that the mean vertical velocity in simulation S3 is overestimated on the windward slope while underestimated over the hilltop. These differences, however, do not lead to significant variations in the predicted deposition pattern. The analysis thus suggests that the reference Cartesian grid with $N_x = 256$, $N_y = 64$, and $N_z = 99$ is sufficient for the purpose of investigating snowfall preferential deposition at the scales of interest.

Acknowledgments
We thank Dirk Goossens for providing us with the experimental data on dust deposition over hills. We are grateful to Ruzica Dadic and all the other anonymous reviewers for their constructive comments to the manuscript. The authors acknowledge the support of the Swiss National Science Foundation (Grant 200021_150146) and the Swiss National Supercomputing Center CSCS (production project s569). The results of the deposition simulations are available online https://www.envidat.ch/dataset/pref-dep-hills).

References

Albertson, J. D., & Parlange, M. B. (1999). Surface length scales and shear stress: Implications for land-atmosphere interaction over complex terrain. *Water Resources Research*, *35*(7), 2121–2132.

Bou-Zeid, E., Meneveau, C., & Parlange, M. B. (2005). A scale-dependent Lagrangian dynamic model for large eddy simulation of complex turbulent flows. *Physics of Fluids*, *17*(2), 025105.

Cermak, J. E. (1984). Physical modelling of flow and dispersion over complex terrain, *Boundary layer structure* (pp. 261–292). Dordrecht: Springer.

Chester, S., Meneveau, C., & Parlange, M. B. (2007). Modeling turbulent flow over fractal trees with renormalized numerical simulation. *Journal of Computational Physics*, *225*(1), 427–448.

Choularton, T. W., & Perry, S. J. (1986). A model of the orographic enhancement of snowfall by the seeder-feeder mechanism. *Quarterly Journal of the Royal Meteorological Society*, *112*(472), 335–345.

Clift, R., Grace, J. R., & Weber, M. E. (2005). *Bubbles, drops, and particles*. New York, London: Courier Corporation.

Comola, F., Kok, J. F., Gaume, J., Paterna, E., & Lehning, M. (2017). Fragmentation of wind-blown snow crystals. *Geophysical Research Letters*, *44*, 4195–4203. https://doi.org/10.1002/2017GL073039

Comola, F., & Lehning, M. (2017). *Energy- and momentum-conserving model of splash entrainment in sand and snow saltation* (Vol. 44, pp. 1601–1609). https://doi.org/10.1002/2016GL071822

Dadic, R., Mott, R., Horgan, H. J., & Lehning, M. (2013). Observations, theory, and modeling of the differential accumulation of Antarctic megadunes. *Journal of Geophysical Research: Atmospheres*, *118*, 2343–2353. https://doi.org/10.1002/2013JF002844

Di Mauro, B., Garzonio, R., Rossini, M., Filippa, G., Pogliotti, P., Galvagno, M., et al. (2018). Saharan dust events in the European Alps: Role on snowmelt and geochemical characterization. *The Cryosphere*, *13*, 1–28.

Diplas, P., Dancey, C. L., Celik, A. O., Valyrakis, M., Greer, K., & Akar, T. (2008). The role of impulse on the initiation of particle movement under turbulent flow conditions. *Science*, *322*(5902), 717–720.

Fang, J., Diebold, M., Higgins, C., & Parlange, M. B. (2011). Towards oscillation-free implementation of the immersed boundary method with spectral-like methods. *Journal of Computational Physics*, *230*(22), 8179–8191.

Garrett, T. J., & Yuter, S. E. (2014). Observed influence of riming, temperature, and turbulence on the fallspeed of solid precipitation. *Geophysical Research Letters*, *41*, 6515–6522. https://doi.org/10.1002/2014GL061016

Gerber, F., Lehning, M., Hoch, S. W., & Mott, R. (2017). A close-ridge small-scale atmospheric flow field and its influence on snow accumulation. *Journal of Geophysical Research: Atmospheres*, *122*, 7737–7754. https://doi.org/10.1002/2016JD026258

Gerber, F., Mott, R., & Lehning, M. (2019). The importance of near-surface winter precipitation processes in complex alpine terrain. *Journal of Hydrometeorology*, *20*(2), 177–196.
Giometto, M. G., Christen, A., Egli, P. E., Schmid, M. F., Tooke, R. T., Coops, N. C., & Parlange, M. B. (2017). Effects of trees on mean wind, turbulence and momentum exchange within and above a real urban environment. *Advances in Water Resources*, *106*, 154–168.
Giometto, M. G., Christen, A., Meneveau, C., Fang, J., Krafczyk, M., & Parlange, M. B. (2016). Spatial characteristics of roughness sublayer mean flow and turbulence over a realistic urban surface. *Boundary-Layer Meteorology*, *160*, 1–28.
Goossens, D. (1996). Wind tunnel experiments of aeolian dust deposition along ranges of hills. *Earth Surface Processes and Landforms*, *21*(3), 205–216.
Goossens, D. (2006). Aeolian deposition of dust over hills: The effect of dust grain size on the deposition pattern. *Earth Surface Processes and Landforms*, *31*(6), 762–776.
Grimmond, C. S. B., & Oke, T. R. (1999). Aerodynamic properties of urban areas derived from analysis of surface form. *Journal of Applied Meteorology and Climatology*, *38*(9), 1262–1292.
Grünewald, T., Schirmer, M., Mott, R., & Lehning, M. (2010). Spatial and temporal variability of snow depth and SWE in a small mountain catchment. *Cryosphere*, *4*(2), 215–225.
Houze, R. A. (2012). Orographic effects on precipitating clouds. *Reviews of Geophysics*, *50*, RG1001. https://doi.org/10.1029/2011RG000365
Huang, N., Sang, J., & Han, K. (2011). A numerical simulation of the effects of snow particle shapes on blowing snow development. *Journal of Geophysical Research*, *116*, D2220. https://doi.org/10.1029/2011JD016657
Kaimal, J. C., & Finnigan, J. J. (1994). *Atmospheric boundary layer flows: Their structure and measurement*. Oxford: Oxford university press.
Kikuchi, T. (1981). A wind tunnel study of the aerodynamic roughness associated with drifting snow. *Cold Regions Science and Technology*, *5*(2), 107–118.
Kim, H. G., Lee, C. M., Lim, H. C., & Kyong, N. H. (1997). An experimental and numerical study on the flow over two-dimensional hills. *Journal of Wind Engineering and Industrial Aerodynamics*, *66*(1), 17–33.
Kok, J. F., Parteli, E. J. R., Michaels, T. I., & Karam, D. B. (2012). The physics of wind-blown sand and dust. *Reports on Progress in Physics*, *75*(10), 106901.
Kolmogorov, A. N. (1941). The local structure of turbulence in incompressible viscous fluid for very large Reynolds numbers. *Doklady Akademii Nauk SSSR*, *30*, 301–305.
Lehning, M., Löwe, H., Ryser, M., & Raderschall, N. (2008). Inhomogeneous precipitation distribution and snow transport in steep terrain. *Water Resources Research*, *44*, W07404. https://doi.org/10.1029/2007WR006545
Lenaerts, J. T. M., Den Broeke, M. R., Berg, W. J., Meijgaard, E. v., & Kuipers Munneke, P. (2012). A new, high-resolution surface mass balance map of Antarctica (1979–2010) based on regional atmospheric climate modeling. *Geophysical Research Letters*, *39*, L04501. https://doi.org/10.1029/2011GL050713
Lilly, D. (1967). The representation of small-scale turbulence in numerical simulation experiments. In *Proc. IBM Scientic Computing Symp. on Environmental Sciences*, New York, pp. 195–210.
List, R., & Schemenauer, R. S. (1971). Free-fall behavior of planar snow crystals, conical graupel and small hail. *Journal of the Atmospheric Sciences*, *28*(1), 110–115.
Loth, E. (2008). Drag of non-spherical solid particles of regular and irregular shape. *Powder Technology*, *182*(3), 342–353.
Magono, C. (1965). Aerodynamic studies of falling snowflakes. *Journal of the Meteorological Society of Japan*, *43*, 139–147.
Mason, P. J., & Thomson, D. J. (1992). Stochastic backscatter in large-eddy simulations of boundary layers. *Journal of Fluid Mechanics*, *242*, 51–78.
Maxey, M. R., & Riley, J. J. (1983). Equation of motion for a small rigid sphere in a nonuniform flow. *Physics of Fluids*, *26*(4), 883–889.
Meneveau, C., Lund, T. S., & Cabot, W. H. (1996). A Lagrangian dynamic subgrid-scale model of turbulence. *Journal of Fluid Mechanics*, *319*, 353–385.
Moin, P., & Kim, J. (1982). Numerical investigation of turbulent channel flow. *Journal of Fluid Mechanics*, *118*, 341–377.
Mott, R., & Lehning, M. (2010). Meteorological modeling of very high-resolution wind fields and snow deposition for mountains. *Journal of Hydrometeorology*, *11*(4), 934–949.
Mott, R., Schirmer, M., Bavay, M., Grünewald, T., & Lehning, M. (2010). Understanding snow-transport processes shaping the mountain snow-cover. *Cryosphere*, *4*(4), 545–559.
Mott, R., Scipion, D., Schneebeli, M., Dawes, N., Berne, A., & Lehning, M. (2014). Orographic effects on snow deposition patterns in mountainous terrain. *Journal of Geophysical Research: Atmospheres*, *119*, 1419–1439. https://doi.org/10.1002/2013JD019880
Nakaya, U. (1954). *Snow crystals: Natural and artificial*. Cambridge: Harvard University Press.
Okin, G. S., Mahowald, N., Chadwick, O. A., & Artaxo, P. (2004). Impact of desert dust on the biogeochemistry of phosphorus in terrestrial ecosystems. *Global Biogeochemical Cycles*, *18*, GB2005. https://doi.org/10.1029/2003GB002145
Orlandini, S., & Lamberti, A. (2000). Effect of wind on precipitation intercepted by steep mountain slopes. *Journal of Hydrologic Engineering*, *5*(4), 346–354.
Orszag, S. A., & Pao, Y. H. (1975). Numerical computation of turbulent shear flows. *Advances in Geophysics*, *18*, 225–236.
Painter, T. H., Deems, J. S., Belnap, J., Hamlet, A. F., Landry, C. C., & Udall, B. (2010). Response of Colorado River runoff to dust radiative forcing in snow. *Proceedings of the National Academy of Sciences of the United States of America*, *107*(40), 17,125–17,130.
Passarelli, R. E., & Srivastava, R. C. (1979). A new aspect of snowflake aggregation theory. *Journal of the Atmospheric Sciences*, *36*(3), 484–493.
Pope, S. B. (2000). *Turbulent flows*. New York: IOP Publishing.
Porté-Agel, F., Meneveau, C., & Parlange, M. B. (2000). A scale-dependent dynamic model for large-eddy simulation: Application to a neutral atmospheric boundary layer. *Journal of Fluid Mechanics*, *415*, 261–284.
Richter, D. H., & Sullivan, P. P. (2013). Momentum transfer in a turbulent, particle-laden Couette flow. *Physics of Fluids*, *25*(5), 53304.
Salesky, S. T., Giometto, M., Chamecki, M., Lehning, M., & Parlange, M. B. (2019). The transport and deposition of heavy particles in complex terrain: An Eulerian model for large eddy simulation. https://arxiv.org/abs/1903.03521
Sato, T., Kosugi, K., Mochizuki, S., & Nemoto, M. (2008). Wind speed dependences of fracture and accumulation of snowflakes on snow surface. *Cold Regions Science and Technology*, *51*(2), 229–239.
Scipión, D. E., Mott, R., Lehning, M., Schneebeli, M., & Berne, A. (2013). Seasonal small-scale spatial variability in alpine snowfall and snow accumulation. *Water Resources Research*, *49*, 1446–1457. https://doi.org/10.1002/wrcr.20135
Sharma, V., Comola, F., & Lehning, M. (2018). On the suitability of the Thorpe-Mason model for calculating sublimation of saltating snow. *Cryosphere*, *12*(11), 3499–3509.
Sharma, V., Parlange, M. B., & Calaf, M. (2016). Perturbations to the spatial and temporal characteristics of the diurnally-varying atmospheric boundary layer due to an extensive wind farm. *Boundary-layer meteorology*, *162*, 1–28.

Simoëns, S., Saleh, A., Leribault, C., Belhmadi, M., Zegadi, R., Allag, F., et al. (2015). Influence of Gaussian hill on concentration of solid particles in suspension inside turbulent boundary layer. *Procedia IUTAM*, *17*, 110–118.

Thomson, D. J. (1987). Criteria for the selection of stochastic models of particle trajectories in turbulent flows. *Journal of Fluid Mechanics*, *180*, 529–556.

Tseng, Y. H., Meneveau, C., & Parlange, M. B. (2006). Modeling flow around bluff bodies and predicting urban dispersion using large eddy simulation. *Environmental Science & Technology*, *40*(8), 2653–2662.

Verlet, L. (1967). Computer experiments" on classical fluids. I. Thermodynamical properties of Lennard-Jones molecules. *Physical Review*, *159*(1), 98.

Vionnet, V., Martin, E., Masson, V., Lac, C., Naaim Bouvet, F., & Guyomarch, G. (2017). High-resolution large eddy simulation of snow accumulation in alpine terrain. *Journal of Geophysical Research: Atmospheres*, *122*, 11,005–11,021. https://doi.org/10.1002/2017JD026947

Voth, G. A., & Soldati, A. (2017). Anisotropic particles in turbulence. *Annual Review of Fluid Mechanics*, *49*, 249–276.

Wang, Z., & Huang, N. (2017). Numerical simulation of the falling snow deposition over complex terrain. *Journal of Geophysical Research: Atmospheres*, *122*, 980–1000. https://doi.org/10.1002/2016JD025316

Weil, J. C., Sullivan, P. P., & Moeng, C. (2004). The use of large-eddy simulations in Lagrangian particle dispersion models. *Journal of the Atmospheric Sciences*, *61*(23), 2877–2887.

Wilson, J. D. (2000). Trajectory models for heavy particles in atmospheric turbulence: Comparison with observations. *Journal of Applied Meteorology and Climatology*, *39*(11), 1894–1912.

Zängl, G. (2008). The temperature dependence of small-scale orographic precipitation enhancement. *Quarterly Journal of the Royal Meteorological Society*, *134*(634), 1167–1181.

Zwaaftink, C. D. G., Diebold, M., Horender, S., Overney, J., Lieberherr, G., Parlange, M. B., & Lehning, M. (2014). Modelling small-scale drifting snow with a Lagrangian stochastic model based on large-eddy simulations. *Boundary-Layer Meteorology*, *153*(1), 117–139.